UNIVERSITÁ DEGLI STUDI DI PADOVA

FACOLTÁ DI INGEGNERIA

Corso di laurea magistrale in: Ingegneria Aerospaziale

Numerical Study of the Catalytic Jump Effect in the IXV-CATE Experiment

Relatore:
Prof. Daniele Pavarin

Correlatori:
Prof. Olivier Chazot
Prof. Jens H. Walther

Laureando:
Ludovico Zanus

Matricola n.:
1036961

A.A. 2013/2014

UNIVERSITÁ DEGLI STUDI DI PADOVA

FACOLTÁ DI INGEGNERIA

Corso di laurea magistrale in: Ingegneria Aerospaziale

Numerical Study of the Catalytic Jump Effect in the IXV-CATE Experiment

Tesi di Laurea Magistrale, Ottobre 2014

LUDOVICO ZANUS

Numerical Study of the Catalytic Jump Effect in the IXV-CATE Experiment

This report was prepared by:
Ludovico Zanus (1036961)

Supervisors:
Daniele Pavarin, Professor at the Industrial Engineering Department of UNIPD
Olivier Chazot, Professor at the Von Karman Institute for Fluid Dynamics
Jens Honore Walther, Professor at the Mechanical Engineering Department of DTU
Advisor:
Fabio Pinna, Research Engineer at the Von Karman Institute for Fluid Dynamics

Dipartimento di Ingegneria Industriale
Università degli studi di Padova
Via Gradenigo 6/a,
35131 Padova
Italy
Tel: +39 049 8277500

Project period:	February 2014- July 2014
Education:	MSc
Field:	Aerospace Engineering
Remarks:	This report is submitted as partial fulfillment of the requirements for graduation in the above education at Padua University.
Copyrights:	

Abstract

Simulations of the surface catalytic effect and catalytic jump effect are done, in the framework of the in-flight CATE experiment on the ESA IXV re-entry vehicle. In order to estimate the phenomenon impact on the overall heat flux experienced at the TPS, different Mach conditions are tested, both with and without catalytic effect. All the cases are investigated by means of 2D simulations, while the study of the Mach 20 condition is also extended to a 3D simulation for comparison. Solutions are obtained using the commercial software CFD++ and the VKI research code COOLFluiD. The results correctly describe the surface catalytic effect, and they make a first step towards a physical simulation of the heat flux jump at the TPS catalytic properties discontinuity. Discrepancies in the codes solutions are found and explained by the different implementation of some specific aerothermodynamic aspects. Finally, the 3D simulation shows the conservative but reasonable choice of a 2D approach.

Acknowledgments

This thesis represents the conclusion of my university studies, and it is an opportunity to say thanks to all the people who helped me to happily reach this goal. First of all I would like to thank Prof. O. Chazot for giving me the possibility to work on the CATE project. Many thanks go to my advisor Fabio Pinna who guided me through the whole work and thesis process, always giving me useful advice. Thanks also to Andrea Lani who revealed me the secret mysteries of COOLFluiD. Moreover, I would like to thank Prof. J. H. Walther for accepting to be my supervisor at DTU and Prof. D. Pavarin for accepting to be my supervisor at Padua University. Then my thought goes to all the important people in my life. For sure I can not find the words to say how happy I am to have met them, so to keep it simple I would just like to give them a hug, one by one.

Abroad...

I would like to say thanks to my friends in Denmark, in particular people from Container F. They were essential to make this experience abroad a wonderful period of my life. There will be always another dinner with them.

In Italy...

Vorrei ringraziare gli aerospaziali, i compagni di università quelli "fighi", per le ore passate negli ultimi banchi delle aule, gli spritz, le partite a qualsiasi cosa, le feste. Gli amici "di Vittorio", perchè anche se non ci si vede spesso i fedeli ai ritrovi non mancano mai, e ci si diverte sempre. "Quei da Maren" per racchiudere gli amici e le amiche di sempre, con i quali si ha condiviso tutto, quelli che non importa dove tu sia, ma quando ritorni senti di essere di nuovo a casa... e niente è cambiato. Infine (non in ordine di importanza, ma per sottolinearla) un pensiero speciale va ai nonni, a mio fratello, a mia mamma e mio papà, semplicemente perchè sono la Mia famiglia e non hanno mai mancato di dimostrarmelo.

Table of Contents

List of Figures

List of Tables

Chapter 1

Introduction

Atmospheric re-entry is a fundamental aspect for lots of applications in future space transportation, including next-generation launchers, planetary exploration, sample-return missions, future generation satellites servicing, cargo and crew space transportation.
Among all the major nations active in the space sector (US, Russia, China, Europe), all have developed re-entry capabilities except Europe. Until now, ESA, the European Space Agency, had only one flight experience in 1998, with the capsule Advanced Reentry Demonstrator (ARD). The ESA's Future Launcher Preparatory Programme (FLPP) was conceived by its Member States in 2003, with the objective of giving Europe an autonomous position among the world's space players in the strategic area of atmospheric re-entry.

1.1 The IXV Mission

After several years of basic research and technology preparatory programs, the European efforts are now focused on the flight verification of such technologies. The Intermediate eXperimental Vehicle (IXV) is an ESA experimental demonstrator project within the FLPP, aimed to develop and test technologies in the field of atmospheric re-entry through a sub-orbital flight of the test vehicle. ESA and its industrial prime contractors Thales Alenia Space Italy, assisted by ASI, CNES, DLR, ESTEC, VKI and other European industry and research organizations, initiated the IXV project at the beginning of 2005 by defining the mission objectives and maturing the design. Now, the assembling phase of the vehicle is almost finished, and the final launch is expected in November 2014.

The IXV main programme idea is to step forward with respect to ARD, by verifying in-flight critical re-entry technologies performance against a wider re-entry corridor, increasing at the same time the system performance in maneuverability, operability and precision landing. The main mission objectives are strictly related to the fundamental physical phenomena and the critical key technologies, whose deep understanding is essential for the reliability and successful realization of future re-entry missions. Among the most important ones are:

- Aerothermodynamics (e.g. real gas effect, material catalysis, laminar to turbulent transition, turbulent heating, ...) - validation of design tools and improvement of design performance, since the current lack of precise knowledge about the gas physics in re-entry conditions requires additional design margins.

- Thermal Protection and Hot Structures - validation of the in flight behavior of ablative and ceramic thermal protection materials and complex design solutions (e.g. thermal expansion, junctions between different materials, gaps etc ...), taking into account the severe thermo-mechanical environmental conditions.

- Guidance Navigation and Control (GNC) - improvement of the guidance algorithms, coupling of inertial measurement units with GPS for navigation. Validation of the flight control system based mainly in aerodynamic shape, flaps and thrusters propulsion.

In order to fully represent the typical conditions of a LEO return mission, IXV reaches a maximum altitude of 412 km, which guarantees an entry velocity at the impact with the atmosphere of 7.5 km/s ($\sim$ Mach 25), at an altitude of 120 km. It is lunched from Kourou (French Guyane) on a VEGA rocket, performing an equatorial trajectory for a total downrange of $\sim$32800 km. The re-entry phase takes place at an angle of attack of 40°, following a trajectory similar to the space shuttle one. This period lasts $\sim$20 minutes and the experiment finally lands in the Pacific Ocean with the aids of a four stages parachute and a recovery subsystem based on inflating balloons.

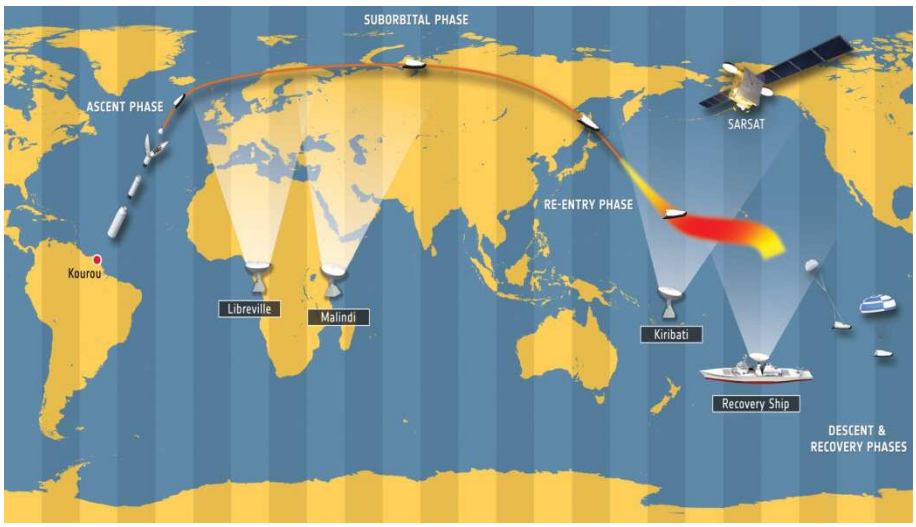

Figure 1.1: *IXV mission.*

1.2 The IXV Vehicle and the CATE Experiment

The IXV vehicle has a conic shape, but with a flat base to ensure lift capability (L/D ratio is equal to 0.7). The spacecraft configuration is aerodynamically stable and characterized by a length of 5 m, width of 2.2 m, height of 1.5 m, and a total weight of $\sim$2 tons. The shape has been defined in order to maximize the internal volume in which the experimental devices and the different subsystems are placed. As stated before, the experiments focus mainly on the aerothermodynamic, thermal protection system and guidance, navigation and control areas.

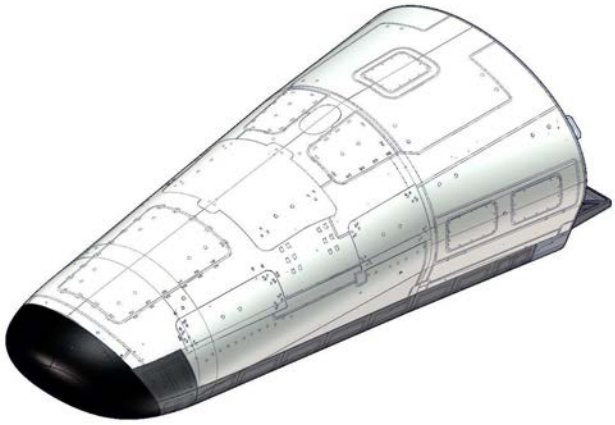

Figure 1.2: *IXV vehicle external layout.*

The Von Karman Institute for fluid dynamics (VKI) is actively involved in the IXV project for the establishment of the aerothermodynamic database (ATDB) and in particular for the design of the Thermal Protection System (TPS). Moreover, it is responsible for the development of an in-flight experiment to asses the Gas-Surface Interaction (GSI) phenomena (mainly catalysis and radiation) along the lifting type trajectory: the "CATalysis Experiment" (CATE). This experiment has been inspired from the similar "Shuttle Catalytic Surface Effects (CSE) Experiment" on the Space Shuttle Orbiter [24]. It consists of two highly catalytic coatings of Mullite, instrumented with thermocouples, and applied at different locations over the low catalytic C-SiC TPS on the windward side of the vehicle. Such coating will promote a catalytic jump due to the wall chemistry discontinuity. In this way it will be possible to study the reaction-diffusion processes associated with the GSI during re-entry conditions.

1.3 The Catalytic Jump Effect

IXV is classified as a low-speed re-entry demonstrator. For this type of vehicles usually reusable passively-cooled TPS are used. In general, these systems are based on catalytic materials, which have the property of promoting the recombination reactions of the atomic species presented in the dissociated gas stream. Since highly exothermic, surface reactions release a considerable amount of energy to the wall, increasing the overall heat flux. When the TPS is built assembling different materials, at their interfaces a discontinuity in the catalytic properties may occur, leading to temperature variations and overheating effects. If the flow at the wall pass from a low catalytic zone to a high catalytic one, a heat flux jump is experienced downstream of the junction as a consequence of the suddenly increased recombination rate of the atoms. This phenomenon is called catalytic jump effect and it has been studied in different flight experiments in the past forty years. The earliest found in literature are the already cited experiments for the Shuttle Orbiter by Stewart and al. [24, 25], followed by the Russian experiments on board of BOR-4 and BOR-5 re-entry vehicleS [29] and the Japanese one in the OREX mission [33]. These experiments proved the low catalytic properties of the based TPS materials, but they were not able to capture accurately the catalytic transition phenomenon, due to problems in sensors resolutions. No experiments of this kind have been flown on European vehicles so far, even if they have been studied and entirely designed. The most recent example is the catalytic experiment for the ESA mission EXPERT [17]. Finally, it has to be pointed out that ground test experiments to investigate these phenomena are very rare. A pioneer example is a work of Sheldahl in 1965 [23]. At VKI Plasmatron (the plasma wind tunnel) catalytic transition tests have been made in the background of the EXPERT and IXV missions, resulting in several publications (refer in particular to F. Panerai [21]).

Figure 1.3: *IXV vehicle: view of the windward part, from where it is possible to see the two patches of the CATE experiment*

1.4 Thesis Objectives and Overview

This work takes part in the CATE experiment and it consists in a numerical study of the catalytic jump effect that occurs at the two patches mounted on board of IXV. The main goal is to perform a complete and reliable CFD analysis at four different Mach conditions (Mach 10, 15, 20, 25) to obtain the estimated heat flux profiles at the vehicle surface. In particular, what happens at the discontinuity between the catalytic properties of the TPS material and the material constituting the patches is investigated. The final data will be used to review the current design and provide input data for further thermal analysis.

The simulations will be run using two software: CFD++ and COOLFluiD, with the purpose of comparing the different aerothermodynaimc models implemented. CFD++ is a commercial software delivered by Metacomp Technologies, able to solve a wide variety of different physical problems in the fluid dynamics area. COOLFluiD is instead a research code for CFD applications, entirely developed at VKI. This platform is able to perform complex multi-physic simulations on unstructured grids, using a wide range of different spatial discretization algorithms and time marching methods. Moreover, the extremely advanced physical models implemented in COOLFluiD are particularly suitable to solve aerothermodynamic problems.

The structure of the thesis follows the logical plan used to carry on the project. In Ch. 2 some fundamental aspects of the physics of high temperature gases are presented, along with the governing equations and the physico-chemical models that permit to correctly describe the interested problem. In Ch. 3 a preliminary 2D study is made in order to compare the two models. A step by step strategy is used, starting with simplified cases without catalytic effect. The idea is to find the precise reasons of eventual disagreements by considering few aspects at a time. In Ch. 4 the catalytic effect at the vehicle surface and the discontinuity of the material catalytic properties are introduced to complete the 2D study. At the end of the chapter a first set of conclusions is presented to summarize the results of the 2D study for all the different Mach conditions. In Ch. 5 a 3D grid convergence study is presented for the only condition of Mach 20 with and without catalytic effect. These simulations will enable the comparison against the 2D simple simulations. In Ch. 6 the final conclusions are given.

Chapter 2

Governing Equations and Physico-chemical Model

Before presenting the equations that govern the physics of the IXV re-entry problem, it is worth pointing out some characteristic aspects of hypersonic fluid dynamics.

2.1 High Temperature Effects in Gas Flows

During atmospheric re-entry the big amount of flow kinetic energy in the hypersonic freestream is converted to internal energy of the gas, across the strong shock wave around the vehicle. Hence, very high temperatures are created in the region between the shock and the body (i.e. the shock layer), especially in the stagnation zone near the nose. At these temperatures the gas does not behave as calorically perfect anymore, this means that the specific heats are no longer constant, and internal energy and enthalpy are not linear functions of the temperature anymore. On the other hand, the gas nature dramatically changes and new phenomena called high temperature effects occur, specifically:

- The internal energy modes of the molecules are excited. This leads the specific heats to become function of the temperature, and the energy and enthalpy to be non-linear functions of the temperature. For air at 1 atm this effect becomes important above a temperature of 800 K.

- As the temperature is further increased, chemical reactions can occur meanly in the form of dissociations and recombinations. In this situation internal energy and enthalpy become functions of both temperature and chemical composition. For air at 1 atm, O_2 starts to dissociate at 2500 K, while N_2 at 4000 K.

- Ionization can occur if the temperature is sufficiently high, in this way a partially ionized plasma is formed and electromagnetic fields and induced forces become important. For air at 1 atm this starts happening at 9000 K, both for oxygen and nitrogen.

- For extremely high temperatures, radiation emitted and adsorbed by the gas can not be neglected, because it changes the energy distribution in the flow field. For air this has to be considered above $\sim$11000 K

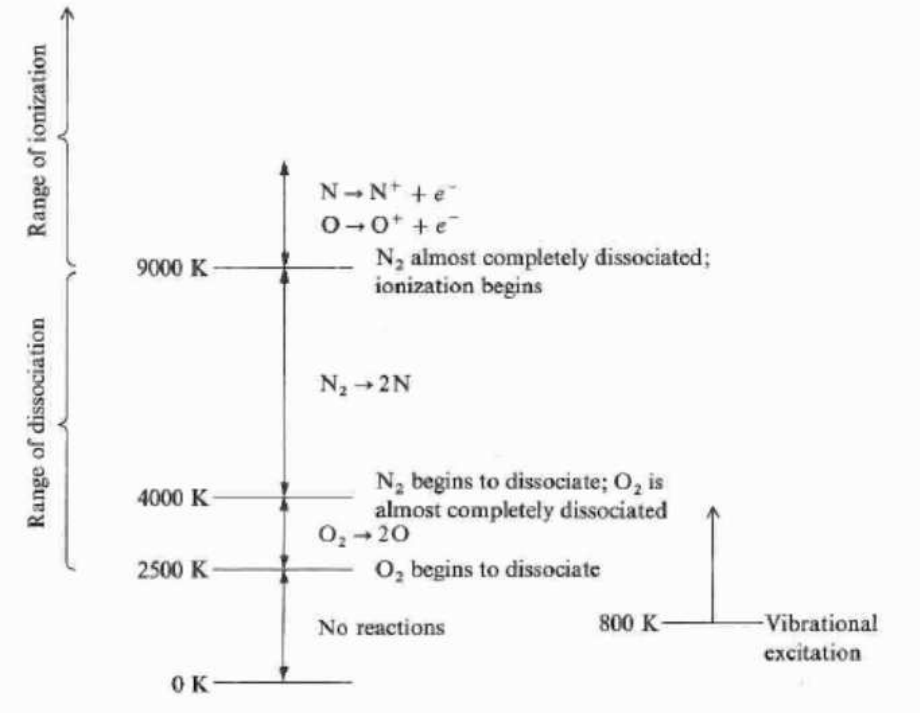

Figure 2.1: *Range for vibrational excitation, dissociation and ionization for air at* 1 *atm. With exception of vibrational excitation (not affected by pressure), these ranges limits decrease if air pressure is lowered [1].*

Moreover, it is worth noticing that in hypersonic regime nonequilibrium conditions can occur. In particular the gas can be in:

- *Thermal nonequilibrium*: the internal energy modes are not in equilibrium with the translational one because on an insufficient number of collisions. The problem is solved by describing the distribution of the particles populations among the internal energy levels and the energy exchange between the different energy modes. This is done by multitemperature models (suitable for near equilibrium situations), or collisional radiative models (good for strong nonequilibrium conditions) [22].

- *Chemical nonequilibrium*: molecular collisions do not have enough time to complete the chemical reactions, so the mixture composition does not correspond to the one at equilibrium conditions for the same values of pressure and temperature. This problem is solved calculating the finite velocity at which reactions occur by using the chemical rate equation.

The opposite conditions are named respectively Thermal Equilibrium and Chemical Equilibrium. A gas is said to be in Thermodynamic Equilibrium if it is both in thermal and chemical equilibrium. For a gas in this situation any two thermodynamic state variables uniquely define its complete thermodynamic state. The IXV vehicle is subjected to conditions typical for low orbit re-entry. The maximum velocity considered in the simulations is about 7.2 km/s, corresponding to a Mach number value of $\simeq 25$. In this high-speed problem nonequilibrium situations are expected, for example across the shock wave where p and T are suddenly increased. Nevertheless, while chemical nonequilibrium is essential for a correct description of the phenomena, previous simulations have shown that thermal equilibrium is a good assumption, at least for the heat flux evaluation. Hence, in this case only one temperature is required to described the populations distribution among the different energy levels.

2.2 Governing Equations

The governing equations state the validity of the basic physical principles of conservation of mass, momentum and energy. Due to the general principle of their derivation, they do not provide all the terms presented in their expressions, but different physico-chemical theories are needed to calculate them. Hence, the problem is closed by the expressions defining the thermodynamics properties (internal energy, enthalpy and specific heat) provided by the statistical and quantum mechanics, the transport properties (viscosity, thermal conductivity, diffusion) provided by the kinetic theory, and the mass production terms provided by the thermo-chemistry. The model presented in this section is the one used in VKI by F. Barbante [2], and it is the base on which COOLFluiD is built. Appropriate comparisons with the CFD++ strategies to model this kind of flow will be pointed out at the end of Ch. 3.

Continuity Equation

The continuity equation can be written as:

$$\frac{\partial \rho}{\partial t} + \nabla \cdot (\rho \vec{V}) = 0 \tag{2.1}$$

where ρ is the mixture density and $\vec{V}$ is the mixture average velocity.

Species Continuity Equation

The continuity equation for each component of the mixture is:

$$\frac{\partial \rho_i}{\partial t} + \nabla \cdot (\rho_i \vec{V}_i) = \dot{\omega}_i \tag{2.2}$$

where ρ_i is the density and $\vec{V_i}$ is the average velocity of the single species i. $\dot{\omega}_i$ is the chemical production term and it describes the rate of production or depletion of species i due to chemical reactions. It is possible to rewrite the equation by decomposing the species average velocity as $\vec{V_i} = \vec{V} + \vec{\mathcal{V}_i}$, with $\mathcal{V}_i$ the diffusion velocity of species i:

$$\frac{\partial \rho_i}{\partial t} + \nabla \cdot (\rho_i \vec{V} + \vec{J_i}) = \dot{\omega}_i \tag{2.3}$$

where the definition of diffusion flux $\vec{J_i} = \rho_i \vec{\mathcal{V}_i}$ has been used.

Momentum Equation

The momentum conservation equation can be written as:

$$\frac{\partial \rho \vec{V}}{\partial t} + \nabla \cdot (\rho \vec{V} \otimes \vec{V}) + \nabla p = \nabla \cdot \bar{\tau} \tag{2.4}$$

where p is the mixture pressure, $\bar{\tau}$ is the viscous stress tensor and external electromagnetic and body forces are neglected.

Energy Equation

The total energy conservation for the mixture of interest is:

$$\frac{\partial \rho E}{\partial t} + \nabla \cdot [(\rho E + p)\vec{V}] - \nabla \cdot (\bar{\tau} \cdot \vec{V}) + \nabla \cdot \vec{q} = 0 \tag{2.5}$$

where E is the total energy per unit mass formed by the sum of the mixture internal energy and the kinetic energy: $E = e + \frac{\|\vec{V}\|^2}{2}$, and $\vec{q}$ is the heat flux. In this case the work done by the body and electromagnetic forces is neglected.

2.3 Thermodynamic Properties

High temperature fluids are in general made of a mixture of different species, and in the pressure and temperature ranges of interest for this kind of problems, each one can be described with good approximation by the perfect gas law:

$$p_i = \rho_i R_i T \tag{2.6}$$

where p_i, ρ_i and R_i are respectively the partial pressure, the partial density and the specific gas constant of the i^{th} species. The mixture pressure p is then calculated by the Dalton's law $p = \sum_i^{Ns} p_i$.

Energy, Enthalpy and Specific Heats

Statistical thermodynamics coupled with quantum physics tell us how to calculate the energy of a gas mixture. Atoms and molecules can store energy in different modes and each one of them is quantized. In an atom it is possible to define two energy modes:

- Translational: associated with the motion of the center of mass
- Electronic: associated with the electrons orbiting around the nucleus

While in a molecule two additional modes has to be taken into account:

- Rotational: associated with the rotation of the molecule around its three orthogonal axes
- Vibrational: associated with the vibration of the atoms forming the molecule, respect their equilibrium position

For a perfect gas the translational mode is independent of the others, and if every diatomic molecule can be modeled as a rigid rotor-harmonic oscillator, all the other internal modes can be considered independent of each other too. Moreover, it is useful to express the energy modes relative to the value they assume at absolute zero, or the zero-point energy state e_0. In this way it is possible to write the energy of an atom as:

$$e_A = e_{tr} + e_{el} + e_0 \tag{2.7}$$

and for a molecule as:

$$e_M = e_{tr} + e_{rot} + e_{vib} + e_{el} + e_0 \tag{2.8}$$

Every energy mode can assume infinite different discrete values, or levels, and each one of them can manifest itself in different states. The number of these states for each energy level is called degeneracy and it is denoted g_i. Hence, the total energy of a system of N particles can be written as:

$$E = \sum_{i=0}^{\infty} \epsilon_i N_i \tag{2.9}$$

where N_i is the number of particles in the i^{th} energy levels and ϵ_i is its energy content. The distribution of the population among the different energy levels is given by statistical thermodynamics and it corresponds to the most probable particle distribution. It is called Boltzmann distribution, it occurs when the system is in thermodynamic equilibrium and its expression is:

$$N_i = N \frac{g_i e^{-\frac{\epsilon}{kT}}}{Q} \tag{2.10}$$

where k is the Boltzmann constant and Q is called the system partition function. Now, substituting Eq. (2.10) in Eq. (2.9), it is possible to express the energy (but the same is for the other thermodynamic properties) in terms of the partition function. The important fact about the partition function is that it is a function of the temperature and volume of

the system, and because the modes are independent it can be written as the product of the partition functions of each energy mode (i.e. for an atom $Q = Q_{tr}Q_{el}$). Once all the different partition functions are computed with the aid of quantum mechanics, the expressions of the energy modes per unit mass are defined as follow [1, 28].

- Transaltional energy
$$e_{tr,i} = \frac{3}{2}R_iT \tag{2.11}$$
- Rotational energy
$$e_{rot,i} = R_iT \tag{2.12}$$
- Vibrational energy
$$e_{vib,i} = R_i\frac{\theta_V}{e^{\frac{\theta_V}{T}} - 1} \tag{2.13}$$
where θ_V is the vibrational characteristic temperature.
- Electronic energy
$$e_{el,i} = R_i\frac{\sum_{k=0}^{\infty} g_k\theta_{E,k}e^{\frac{-\theta_{E,k}}{T}}}{\sum_{k=0}^{\infty} g_k e^{\frac{-\theta_{E,k}}{T}}} \tag{2.14}$$
where $\theta_{E,k}$ is the characteristic electronic temperature for level k.

The enthaply is simply computed by adding to the energy the extra term: R_iT. Thus the mixture energy and enthalpy per unit mass are obtained from the expressions:

$$e = \sum_{i=1}^{Ns} x_ie_i \qquad h = \sum_{i=1}^{Ns} x_ih_i \tag{2.15}$$

where x_i is the mass fraction of species i.

Finally, the specific heats for the mixture are derived by means of the formulae:

$$c_v = \left(\frac{\partial e}{\partial T}\right)_v = \sum_{i=1}^{Ns}\left[\left(\frac{\partial x_i}{\partial T}\right)_v e_i + x_i\left(\frac{\partial e_i}{\partial T}\right)_v\right] \tag{2.16}$$

$$c_p = \left(\frac{\partial h}{\partial T}\right)_v = \sum_{i=1}^{Ns}\left[\left(\frac{\partial x_i}{\partial T}\right)_p h_i + x_i\left(\frac{\partial h_i}{\partial T}\right)_p\right] \tag{2.17}$$

Nevertheless, in chemical non equilibrium conditions, the gas composition is a function not only of the thermodynamic variables, but also of the position and the previous flow history. Thus the derivative of x_i is not uniquely defined, and the specific heats reduce to the only "frozen" component.

2.4 Transport Properties

In order to close the problem the knowledge of diffusion fluxes J_i, stress tensor $\bar{\tau}$ and heat flux $\vec{q}$ is necessary. These fluxes are associated with the transport respectively of mass, momentum and energy, and they are the result of the gradients in the macroscopic physical properties of composition, velocity and temperature. The complete derivation of their expressions can be found in [6, 7], here only the derivation method and the final results are summarized.

The transport fluxes formulation requires the knowledge of the distribution function $f_i(\vec{r}, \vec{c}, I, t)$, which, once integrated, gives the amount of i species particles in a certain position, with a certain velocity and internal state. Its behavior is described by the Boltzmann equation, whose solution is given by Maxwell for a gas in thermodynamic equilibrium and by Chapman-Enskog for nonequilibrium conditions. Inserting the solution in the fluxes definitions it is possible to obtain the following expressions.

Diffusion Flux

Diffusion is caused by gradients in chemical composition, in pressure and in temperature, and difference on the body forces acting on each species (the latter three usually negligible). The flux can be written as:

$$\vec{J_i} = -\rho_i \left(\sum_{j=1}^{Ns} D_{i,j} \vec{d_j} + D_i^T \nabla log T \right) \tag{2.18}$$

where $D_{i,j}$ are the multicomponent diffusion coefficients and D_i^T the thermal diffusion coefficients, computed by polynomial expansions and $\vec{d_j}$ is the vector of the driving forces. Usually in most of the other models another expression is used for the diffusion flux due to the high computational cost in evaluating the diffusion coefficients. It is based on some kind of Fick's law and reads:

$$\vec{J_i} = -\rho D_i^m \nabla x_i \tag{2.19}$$

where D_i^m is a suitable multicomponent binary diffusion coefficient. This formula is less accurate because it does not satisfy, in general, the constrain of mass conservation.

Viscous Stress Tensor

The viscous stress tensor takes the form:

$$\bar{\tau} = \mu \left(\nabla \vec{V} + \nabla \vec{V}^T \right) + \left(\eta - \frac{2}{3} \mu \right) \nabla \cdot \vec{V} \bar{I} \tag{2.20}$$

where μ is the coefficient of shear viscosity and η is the coefficient of volume viscosity. The former is determined by polynomial expansion, while the latter is usually neglected because the lack in necessary data to correctly compute it.

Heat Flux

The expression of the heat flux vector can be written as:

$$\vec{q} = -\lambda \nabla T + \sum_{i=1}^{Ns} h_i \vec{J}_i - p \sum_{i=1}^{Ns} D_i^T \vec{d}_i \tag{2.21}$$

where λ is the coefficient of partial thermal conductivity and is computed once more by polynomial expansion. The first term in the equation represents the Fourier's law, the second one the transfer of enthalpy due to particle diffusion and the third one the Dufour effect, i.e. the heat diffusion due to gradients in concentration.

2.5 Chemistry

A reaction occurring in one step, also called elementary reaction (identified with the index r), can be written in general as:

$$\sum_{i=1}^{Ns} \nu'_{ir} X_i \leftrightarrows \sum_{i=1}^{Ns} \nu''_{ir} X_i \tag{2.22}$$

where X_i is a symbol for the i species, ν'_{ir} is the stoichiometric coefficient of the i^{th} reactant and ν''_{ir} is the stoichiometric coefficient of the i^{th} product. As the formula shows, an elementary reaction can proceed in both directions, and it is in chemical equilibrium when dissociation and recombination are perfectly balanced. The net rate of production of species i is calculated by summing the contributions from all the Nr elementary reactions, and it is described by the Law of Mass Action [28]:

$$\dot{\omega}_i = M_i \sum_{r=1}^{Nr} (\nu''_{ir} - \nu'_{ir}) \left\{ k_{fr} \prod_{j=1}^{Ns} \left(\frac{\rho_j}{M_j} \right)^{\nu'_{jr}} - k_{br} \prod_{j=1}^{Ns} \left(\frac{\rho_j}{M_j} \right)^{\nu''_{jr}} \right\} \tag{2.23}$$

where k_{fr} and k_{br} are respectively the forward and backward reaction rate for the r^{th} reaction. These two parameters are linked by the relation $K_{cr} = k_{fr} \cdot k_{br}$, where K_{cr} is the equilibrium constant for the r^{th} elementary reaction and it is a function only of the temperature. Thus, only one of the reaction rate needs to be defined and the semi-empirical formulation, known as Arrhenius Law, provides the expression:

$$k_{fr} = A_r T^{\eta} e^{-\frac{\Theta_r}{T}} \tag{2.24}$$

with A_r and η constant coefficients and Θ_r the activation temperature for the r^{th} reaction. Values of k_{fr} are usually computed by fitting experimental data, but the difficulty in doing these evaluations leads to large differences among different authors.

Air Chemistry Model

Air is a mixture of different gases. At ambient temperature it is composed of molecular nitrogen (N_2), molecular oxygen (O_2), carbon dioxide (CO_2), argon (Ar) and other minor gases. For the kind of problem taken into account in this work, it is possible to assume air made only of N_2 and O_2. Nevertheless, as the temperature increases, chemical reactions occur and the air chemical composition changes. Two kinds of reactions are considered in this model: thermal dissociation of molecules and bimolecular exchange. All the reactions involving ionization are neglected, because the improved model accuracy does not vary significantly the results, as demonstrated in previous studies. For this reason, an air mixture of five species (air-5): $N_2,\ O_2,\ NO,\ O,\ N$, is sufficient to describe all the chemical reactions that take place in the hot environment around the vehicle during the re-entry phase. The reactions considered are collected in Table 2.1.

Thermal dissociation	Bimolecular exchange
$O_2 + M \leftrightarrows O + O + M$	$O_2 + N \leftrightarrows NO + O$
$N_2 + M \leftrightarrows N + N + M$	$N_2 + O \leftrightarrows NO + N$
$NO + M \leftrightarrows N + O + M$	

Table 2.1: *Chemical reactions for air-5 model. M is a third body component (i.e. anyone of the five species) which collides with the molecules, but it does not change during the reaction.*

The parameters that compute the forward rate coefficients, thus the velocities at which reactions take place, are taken from Park [5] and they are collected in Table 2.2. The same chemical model and the same rate coefficients are used in both the codes.

Reaction	A_r	η	$\Theta_r\ [K]$
$N_2 + M \leftrightarrows 2N + M \quad (M = N, O)$	$3.00 \cdot 10^{22}$	-1.60	113200
$N_2 + M \leftrightarrows 2N + M \quad (M = N_2, O_2, NO)$	$7.00 \cdot 10^{21}$	-1.60	113200
$O_2 + M \leftrightarrows 2O + M \quad (M = N, O)$	$1.00 \cdot 10^{22}$	-1.50	59360
$O_2 + M \leftrightarrows 2O + M \quad (M = N_2, O_2, NO)$	$2.00 \cdot 10^{21}$	-1.50	59360
$NO + M \leftrightarrows N + O + M \quad (M = N_2, O_2)$	$5.00 \cdot 10^{15}$	0.00	75500
$NO + M \leftrightarrows N + O + M \quad (M = N, O, NO)$	$1.00 \cdot 10^{15}$	0.00	75500
$N_2 + O \leftrightarrows NO + N$	$5.69 \cdot 10^{12}$	0.42	42938
$O_2 + N \leftrightarrows NO + O$	$2.49 \cdot 10^{9}$	1.18	4005.5

Table 2.2: *Park's coefficients for the reactions of interest [5].*

Chapter 3

Preliminary 2D Study

In this chapter the general implementation of the 2D study and the presentation of some preliminary results are discussed. In the first part, the mesh generation and its characteristics are explained along with the description of all the different boundary conditions. Then, some simplified 2D cases are considered, with the idea of analyzing few aspects at the same time. This is done in order to make easier and clearer the investigation of possible differences between the aerothermodynamic models used in CFD++ and COOLFluiD. The codes use both a finite volume solver with a second order scheme.

3.1 Mesh Generation

In order to study the 2D case, a domain for previous studies on IXV is used. The geometry is obtained by cutting the three dimensional flow field around the windward part of the vehicle with a longitudinal plane perpendicular to the TPS surface and passing through the center line of the vehicle.

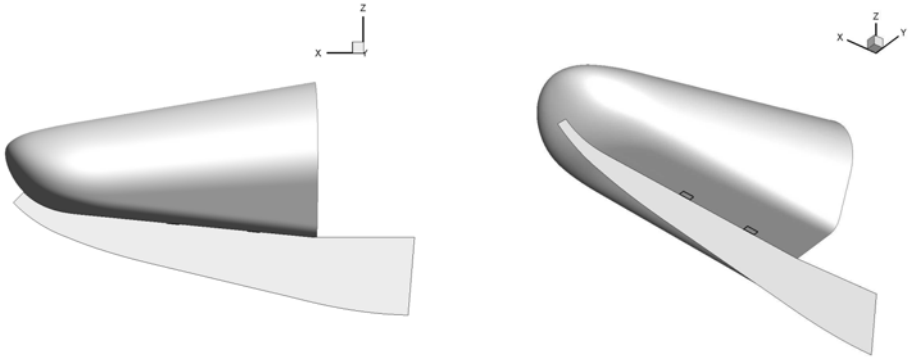

(a) Lateral view. **(b)** Perspective view from the bottom.

Figure 3.1: *Visualization of the 2D domain on the partial 3D IXV model.*

In this way the wall edge is defined, while the others are drawn respectively along the

stagnation line, following the shock line at a suitable distance and closing the domain at the back limit of the vehicle. Figure 3.1 shows the 2D flow field together with a IXV 3D model. In this picture the 3D model is cut before its effective end, so the 2D domain is actually extended over the complete vehicle length. It has to be known that the vehicle has a symmetric geometry, but it is not symmetric if the two patches disposition is considered. In fact, the longitudinal central axis of the patches does not correspond to the center line of the vehicle, but it is shifted by 3.9 cm. Thus the position of the patches on the 2D domain is not exactly the real one, even if the relative error can be considered negligible. Further implications concerning the 2D domain position will be treated in Sec. 3.2 where the boundary conditions are explained.

To impose the boundary condition on the velocity, the 2D domain is rotated conveniently and displayed with the relative reference system as shown in Figure 3.2. In this way the x-axis points along the stagnation line and the y-axis is the orthogonal one towards the vehicle backward direction. The velocity vector is now reduced to only one component in the x direction. Six boundary regions are defined on the domain edges: inlet, outlet, wall, patch1, patch2 and symmetry. Each one of them corresponds to a different imposition of the boundary conditions.

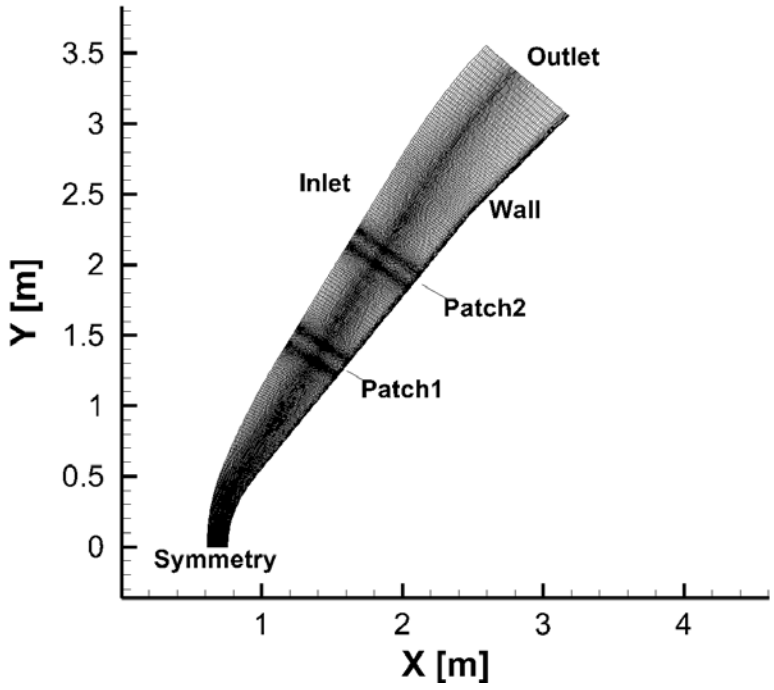

Figure 3.2: *Full domain 2D mesh with relative boundary regions.*

The 2D mesh is built using the software ICEM from the ANSYS suite, while to set the boundary conditions and to export in the suitable final mesh format, GAMBIT is

used. The domain is discretized with quadratic elements because they are more accurate in problems regarding heat flux computation. The total number of elements is around 67000. Particular care is spent refining the zones around the two patches, where a discontinuity in the heat flux is expected, along the shock line, where a discontinuity in the flow properties occurs, and in the boundary layer, where viscous effects take place (Figure 3.3). The same mesh is used for all the 2D simulations, even if the shock position changes according to the Mach. Nevertheless, not differences have been seen in a test solution with and without shock refinement, thus the grid can be considered sufficiently fine and suitable for all the flow regimes.

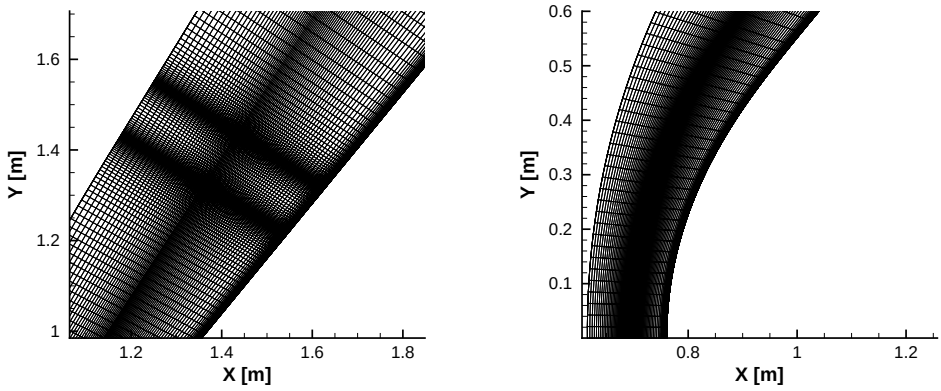

(a) Particular of patch 1.

(b) Particular of the shock close to the stagnation point.

Figure 3.3: *Mesh refinements zoom of critical domain parts.*

3.2 Boundary Conditions

The boundary conditions presented in this section are applied to all 2D simulations, with the exception of the condition at the wall when the catalytic effect is introduced. In this case the proper numeric setting will be explained in Ch. 4. Particular attention is given here at the description of the boundary condition at the vehicle surface, because it is fundamental for a correct estimation of the wall heat flux. Hence, the six regions defined at the 2D domain edges correspond to the following conditions:

Inlet

At the inlet boundary the freestream parameters are imposed. These are the freestream pressure, temperature, velocity, density and mixture composition. The flow is considered laminar, because for re-entry vehicles usually transition to turbulence occurs approximately at around 60 to 40 km of altitude, and in general it starts in the rear part of the body [12]. Thus, for the Mach conditions taken into account in this project, the laminar

regime is a reasonable assumption. Four flow conditions are investigated, corresponding to Mach number 10, 15, 20 and 25. These are related to four different situations IXV has to experience along its re-entry trajectory. The flow is fully described by the project data given in terms of Mach number, freestream pressure and temperature. The other quantities are calculated using the Mach definition expression and the perfect gas law. They are collected in Table 3.1.

Mach	Pressure [Pa]	Temperature [K]	Velocity [m/s]	Density [kg/m^3]
10	61.19	267.41	3278.40	7.9705e-4
15	26.30	250.61	4720.62	3.6550e-4
20	6.13	222.44	5980.10	9.5991e-5
25	1.87	205.73	7188.90	3.1661e-5

Table 3.1: *Freestream flow conditions defining the four test cases studied in the 2D simulations.*

The freestream gas mixture is considered composed only by molecular nitrogen and molecular oxygen. In particular the mass fraction values used are $x_{N_2} = 0.767$ and $x_{O_2} = 0.233$.

Outlet

At the outflow boundary no numerical conditions are set. At a supersonic outflow, in fact, no signals are allowed to travel back into the flow domain, thus no quantities are specified in this region.

Symmetry

At the edge along the stagnation line an axis-symmetric condition is imposed. This means that the 2D simulation represents the equivalent case of a flow around a 3D object, whose volume is described by the revolution of the 2D domain around the x-axis. This would lead to a symmetric conic shape vehicle with a geometry very different from the real one. Considering the flatness of the IXV bottom part, it would make sense also to run a simply 2D simulation. In this way the simulation would be equivalent to a flow over a ramp, whose profile is obtained by extruding the 2D domain. Nevertheless, it is customary in these studies to use the axis-symmetric approach, because it represents a more conservative solution. In fact, given the same flow parameters, the shock is placed closer to the body surface in the cone configuration rather than in the ramp one, leading to higher values of temperature and heat flux. Hence, the axis-symmetric condition is used with the idea of considering the worst case scenario. The solution of the 3D simulation will eventually show how important these differences will be. Finally, the fact that the patches do not lie on the center line of the vehicle introduces another approximation, because possible phenomena due to the crossflow are neglected.

Wall

In order to correctly compute the heat exchange between the gas and the vehicle surface, it is necessary to correctly define the thermal state of the TPS and understand the different contributions that form the overall heat flux. In general, the total energy flux at a point (energy per second per unit area) for a high temperature chemical reacting gas is computed by the sum of three terms. In stationary conditions, the energy is transported by thermal conduction ($\vec{q}_c$), by diffusion of species ($\vec{q}_d$) and by radiation ($\vec{q}_r$). Hence:

$$\vec{q}_{gas} = \vec{q}_c + \vec{q}_d + \vec{q}_r \tag{3.1}$$

For LEO re-entry missions with velocity smaller than approximately 8 km/s (which is also the case of the IXV mission), the absorption and emission of radiation energy in the gas can be neglected [11]. The other two terms on the RHS of Eq. (3.1) instead can be more precisely described as:

- *conductive heat flux*: $\vec{q}_c = -\lambda \nabla T$, where λ is the mixture thermal conductivity
- *diffusive heat flux*: $\vec{q}_d$ due to the diffusion of each species i carrying its enthalpy h_i through the gas. The energy flux caused by diffusion of species i can be expressed as:

  $$\vec{q}_{d,i} = \rho_i \vec{\mathcal{V}}_i h_i \tag{3.2}$$

  where ρ_i is the density and $\vec{\mathcal{V}}_i$ is the diffusion velocity of species i. It has to be noticed that the product $\rho_i \vec{\mathcal{V}}_i$ corresponds exactly to the mass flux of species i, $\vec{J}_i$. Thus, for all the n species, the energy flux becomes:

  $$\vec{q}_d = \sum_{i=1}^{n} \vec{q}_{d,i} = \sum_{i=1}^{n} \rho_i \vec{\mathcal{V}}_i h_i = \sum_{i=1}^{n} \vec{J}_i h_i \tag{3.3}$$

Hence, substituting in Eq. (3.1), the total energy flux at a point for the gas mixture takes the form:

$$\vec{q}_{gas} = -\lambda \nabla T + \sum_{i=1}^{n} \vec{J}_i h_i \tag{3.4}$$

The boundary condition at the wall is derived considering the thermal balance between the surface and the flow that surrounds it. In a general case this is written as:

$$\vec{q}_w = \vec{q}_{gas} + \vec{q}_{wr} \tag{3.5}$$

where $\vec{q}_w$ is the net heat transfer into the body surface, $\vec{q}_{gas}$ is the heat flux from the gas calculated before, and $\vec{q}_{wr}$ is the heat flux radiated away from the surface (Fig. 3.4). The latter term can be expressed explicitly by the Stefan-Boltzmann law:

$$\vec{q}_{wr} = \varepsilon \sigma T_w^4 \tag{3.6}$$

where ε is the surface emissivity (always equal to 0.8 in this problem), σ is the Stefan-Boltzmann constant ($\sigma = 5.67 \cdot 10^{-8}$ W$/m^2K^4$) and T_w is the wall temperature.

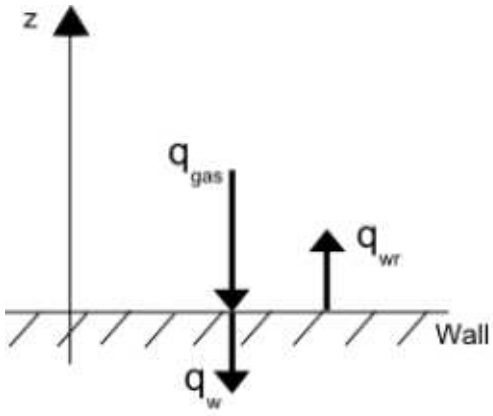

Figure 3.4: *Schematic description of the thermal balance at the wall surface.*

In the design process it is interesting the situation where $\vec{q}_w = 0$, this means that there is not net energy flux through the wall, and the heat released by the gas into the surface is exactly balanced by the heat radiated away from the surface. This condition is called *radiative equilibrium wall*, and it allows to calculate the maximum temperature to be expected locally, i.e. the *radiation-adiabatic wall temperature*, T_{ra}. Considering this case in Eq. (3.5), and substituting the terms respectively with Eq. (3.4) and Eq. (3.6), the final boundary condition in scalar form becomes:

$$0 = -\lambda \frac{\partial T}{\partial z} + \sum_{i=1}^{n} h_i J_{i,z} + \varepsilon \sigma T_w^4 \tag{3.7}$$

where z is the direction normal to the wall, and $J_{i,z}$ is the flux component in this direction.

The surface-radiation cooling is the basic mechanism used to decrease the wall temperature in high-speed vehicles, operating in the earth atmosphere at speed below 8 km/s. It is very effective, and it can cool the surface to temperature which present-day TPS can cope with, without additional cooling. The radiative equilibrium assumption can not be verified in ground-test facilities, mainly due to the limitations in simulating the near-wall viscous-flow and thermo-chemical phenomena at a representative Reynolds number. The only experimental data that can show, at least partly, the correct approximation of the radiation-adiabatic surface to the reality are the Space Shuttle flight data [30, 31], and the result of a numerical study by Wüthrich, Sawley and Perruchoud [32]. The measured and computed temperature are in very good agreement, hence the heat flux into or out of the wall has to be small, i.e. $\vec{q}_w \simeq 0$. Thus, it is possible to say that the radiation-adiabatic surface condition is not a bad approximation of reality, at least for re-entry vehicles with a TPS like the Space Shuttle one. Moreover, the radiation-adiabatic temperature represents a conservative estimate of the wall temperature, and the real temperature in any case lies close to it, i.e. $T_w \approx T_{ra}$.

Patch1 and Patch2

In the preliminary 2D study the catalytic effect is not considered, thus there is no difference between the wall condition imposed on the patches and the one on the rest of the TPS. In other words, the presence of the patches is irrelevant in this situation.

3.3 Preliminary 2D Results

In this preliminary study only the conditions at the lowest and highest Mach are considered as representative situations of the extreme environmental states. The first case taken into account is at Mach 25, where, compared to the other Mach conditions, the temperature field presents the highest values, the gas chemistry is the most active and the gas transport properties have the widest range of variability.

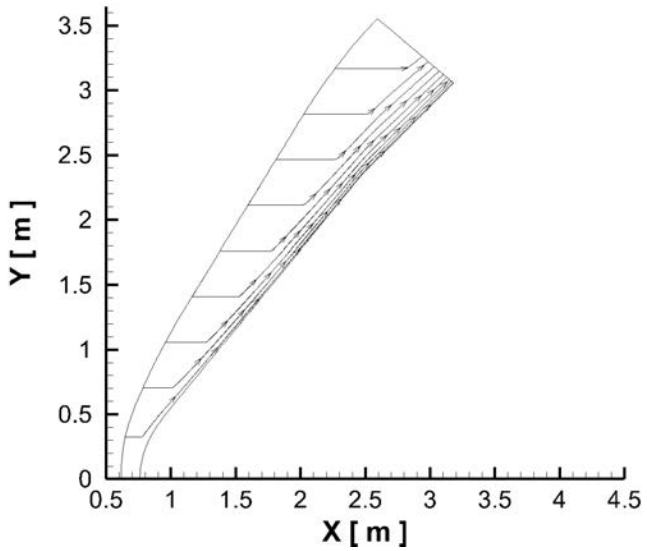

Figure 3.5: *Streamlines for the Mach 25 case with isothermal boundary condition at the vehicle surface (T_w=1000 K).*

Initially, the vehicle surface is considered isothermal to avoid the further complexity of the radiative wall condition. This consists indeed in an iterative solution of isothermal problems, until the wall thermal balance is satisfied. An indicative temperature of 1000 K is set at the vehicle surface for the isothermal case, which is not very far from the expected real temperature. Firstly, the dynamic of the flow is analyzed looking at the velocity streamlines (Figure 3.5). With this domain orientation the flow starts horizontal at the freestream, until the shock wave is encountered. After the shock, the fluid is forced to follow the vehicle surface, so it turns and leaves at the outlet boundary. Hence, at a given position in the shock layer the flow is characterized by a convection component

in the direction tangential to the wall, and a diffusive component, which determines the movement of the single species inside the mixture. This is the general flow behavior in this 2D problem and it is the same for all the different Mach conditions.

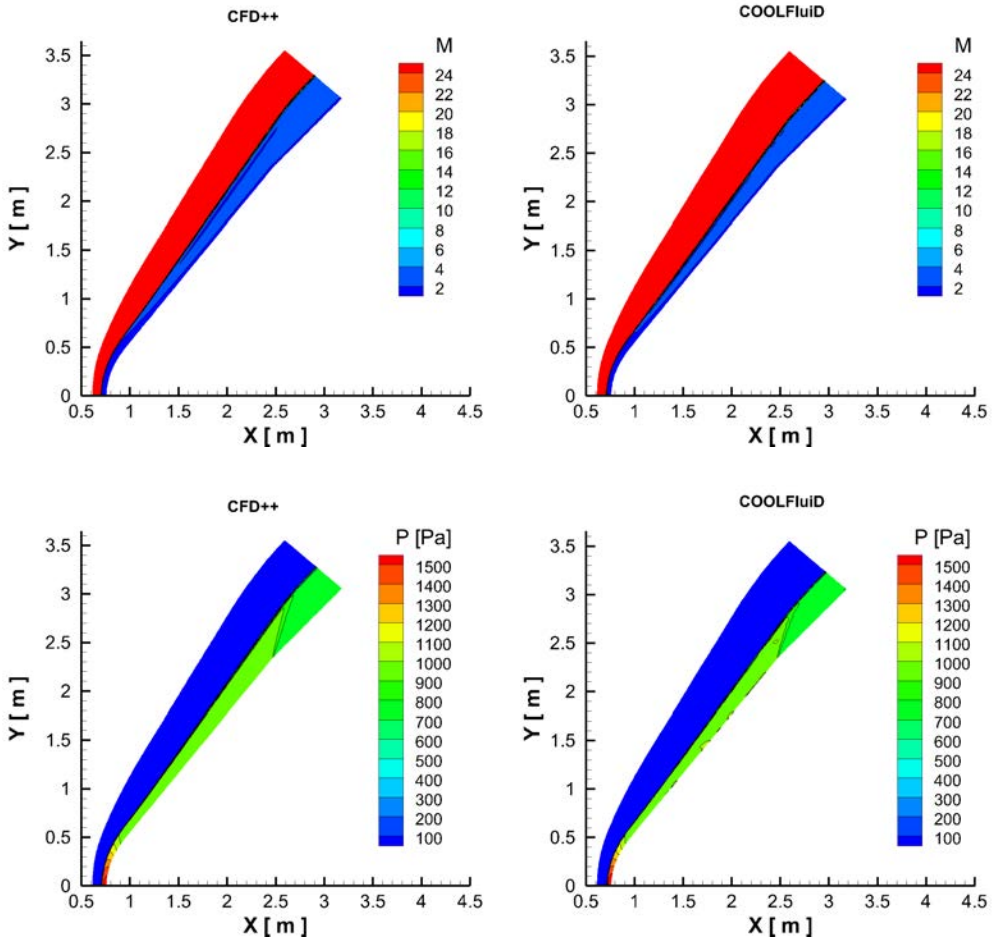

Figure 3.6: *Mach and pressure fields for the Mach 25 case with isothermal boundary condition at the vehicle surface (T_w=1000 K): comparison between CFD++ and COOLFluiD.*

In Figure 3.6 the comparison of the Mach and pressure fields between the two software solutions is shown. No appreciable differences in the quantities values are noticed, but the shock is placed slightly closer to the wall in the COOLFluiD solution. More relevant discrepancies are found instead in the temperature field. As it is possible to see from Figure 3.7, COOLFluiD gives a lower temperature in the shock layer, with an average difference in the center part of about 2000 K.

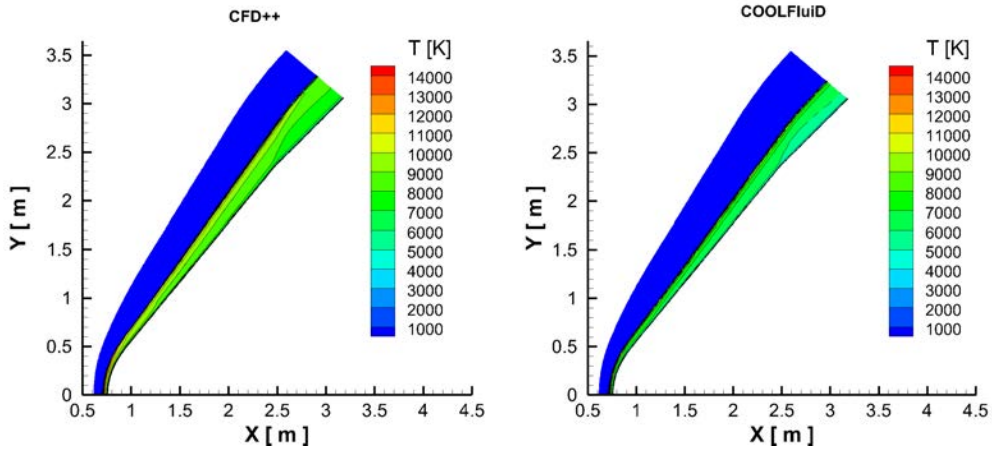

Figure 3.7: *Temperature field for the Mach 25 case with isothermal boundary condition at the vehicle surface (T_w=1000 K): comparison between CFD++ and COOLFluiD.*

A zoom in the stagnation region (Figure 3.8) highlights this temperature behavior, in fact the extremely hot zone between the shock wave and the vehicle nose is more extended in the CFD++ solution both along and across the shock layer.

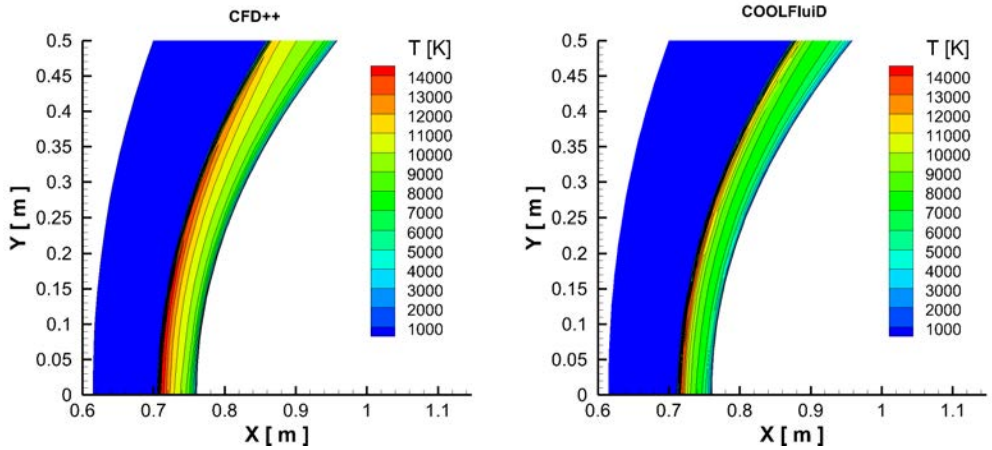

Figure 3.8: *Zoom of the temperature field at the stagnation region for the Mach 25 case with isothermal boundary condition at the vehicle surface (T_w=1000 K): comparison between CFD++ and COOLFluiD.*

Nevertheless, the imposition of a fix temperature at the wall forces the temperature to decrease as the flow goes closer to the surface. A bigger gradient is expected in the CFD++ case, but the difference in the two solutions temperatures becomes smaller and smaller as the wall is approached. In order to calculate the heat flux, also the contribution

from the enthalpy of the different species is important, thus a comparison between the species distributions is considered in Figure 3.9 and Figure 3.10.

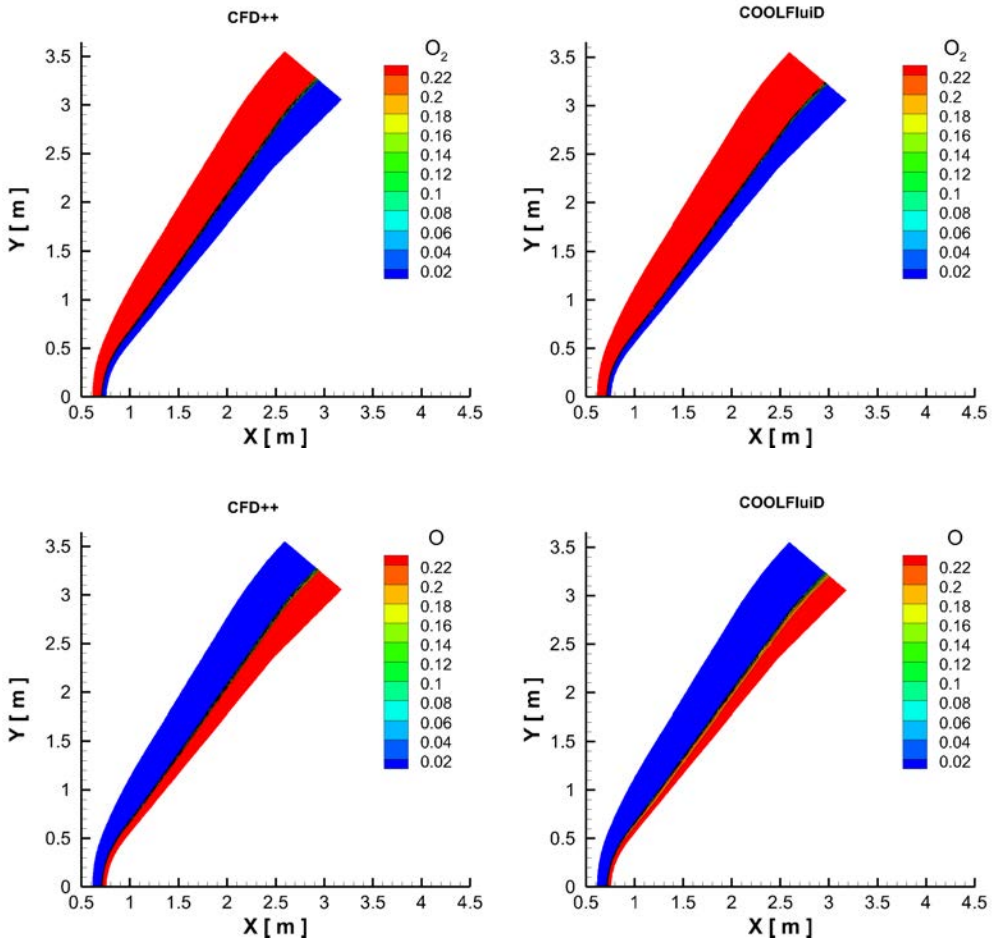

Figure 3.9: *Distribution of the O_2 and O species mass fractions for the Mach 25 case with isothermal boundary condition at the vehicle surface (T_w=1000 K): comparison between CFD++ and COOLFluiD.*

From the pictures it is clear that there is a good agreement between the codes about the treatment of the oxygen chemistry, in fact no considerable variations occur in the mass fraction distributions of O and O_2. On the contrary, the reactions involving nitrogen give as result very different distributions of the N_2, N and NO species, specially outside the stagnation zone. In particular, CFD++ presents in general a higher amount of molecular nitrogen, which means less dissociations or more recombinations, compared to the COOLFluiD solution. Moreover, the NO species is not present at all in the CFD++ solution (maximum values in the order of 10^{-10} are found), while in COOLFluiD it appears mostly along the shock line, even if in small quantity.

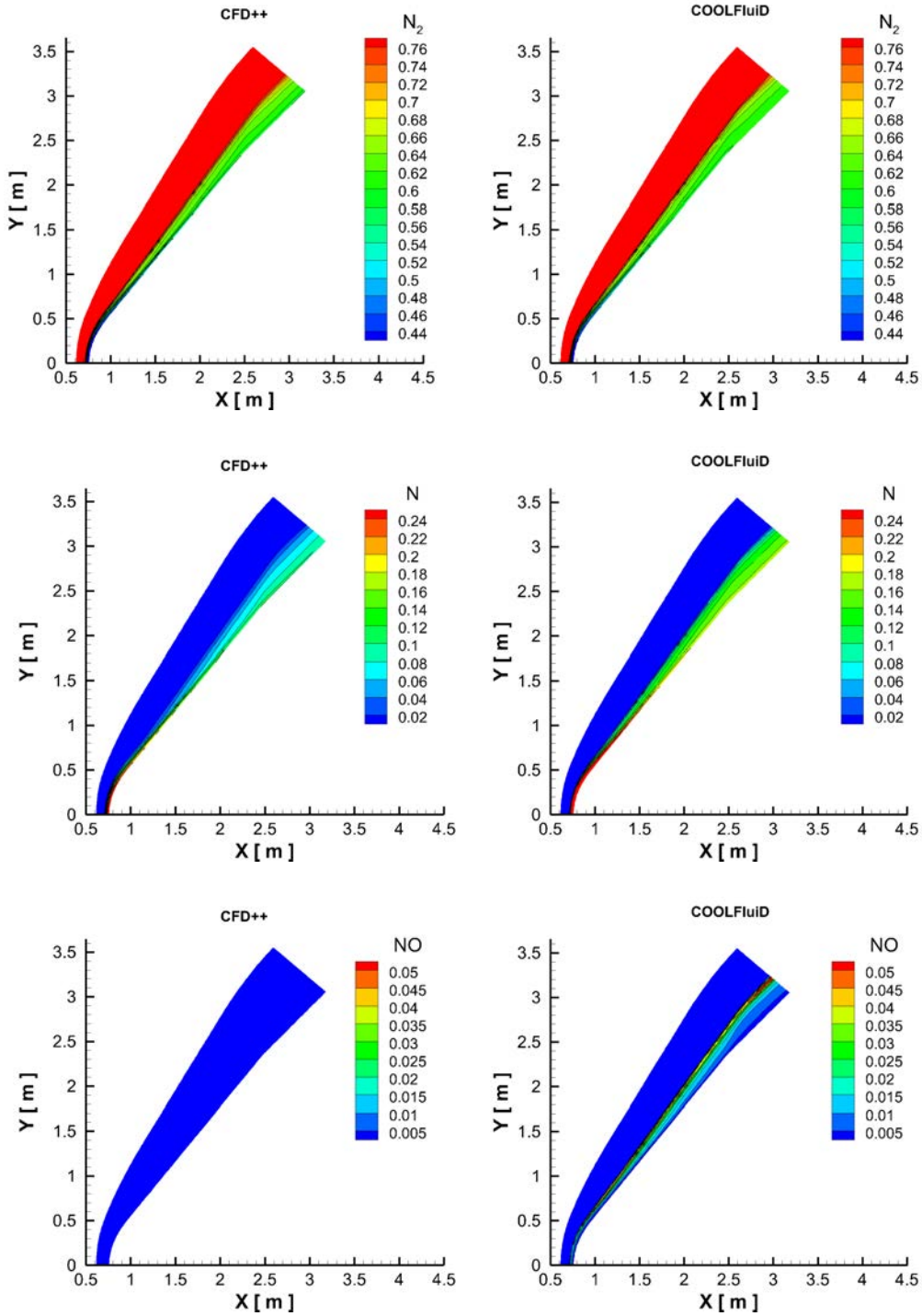

Figure 3.10: *Distribution of the N_2, N and NO species mass fractions for the Mach 25 case with isothermal boundary condition at the vehicle surface (T_w=1000 K): comparison between CFD++ and COOLFluiD.*

There is a strong relation between these processes of dissociation and recombination and the temperature distribution, but the mixture composition is not uniquely defined by the thermodynamics, as it is in chemical equilibrium, it depends also on the position and on the previous flow history. From one side the reaction rates depend on the local temperature, but on the other side the heat absorbed or released in the reactions affects the temperature distribution in the flowfield, so the chemical composition is calculated by an iterative process until convergence is reached. Recombination and dissociation are respectively exothermic and endothermic reactions, thus the bigger amount of atomic particles in COOLFluiD explains why its temperature field is colder than the one calculated by CFD++.

If the less critical case of Mach 10 is considered, a good agreement is found not only in the Mach and pressure solutions, but this time also in the temperature distribution, as Figure 3.11 shows. The temperature is much lower in the shock layer compared to the Mach 25 case (around 3200 K against 9000 K), and the reactions are now concentrated only in the stagnation region where the highest temperature values occur. There are still no relevant differences in the treatment of the oxygen chemistry, while the pictures of the populations involving nitrogen reveal once again disagreements (Figure 3.12). The general behavior of COOLFluiD in calculating higher quantities of N and NO is still present, even if maximum values are low and located in the confined stagnation region close to the surface. It is interesting at this point to compare the wall heat flux for the two cases illustrated so far. Figure 3.13 shows the comparisons between the heat flux profiles along the vehicle surface, calculated by the two software.

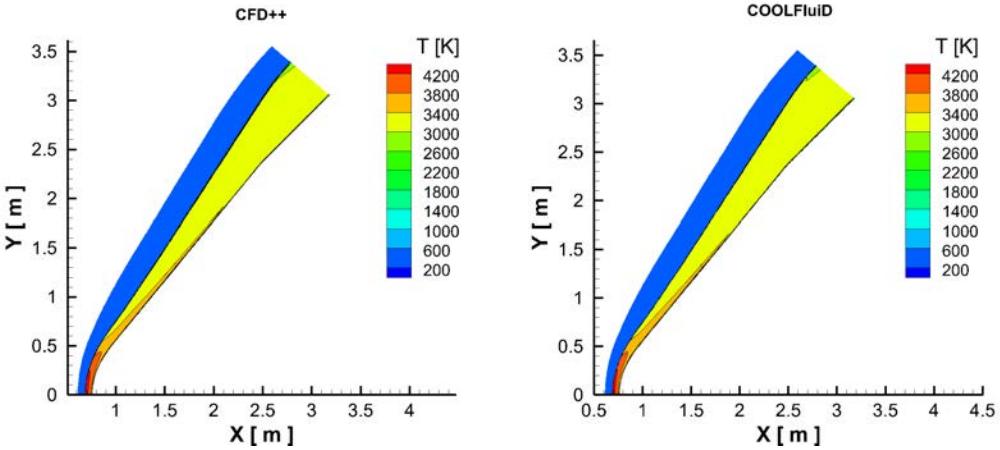

Figure 3.11: *Temperature field for the Mach 10 case with isothermal boundary condition at the vehicle surface (T_w=1000 K): comparison between CFD++ and COOLFluiD.*

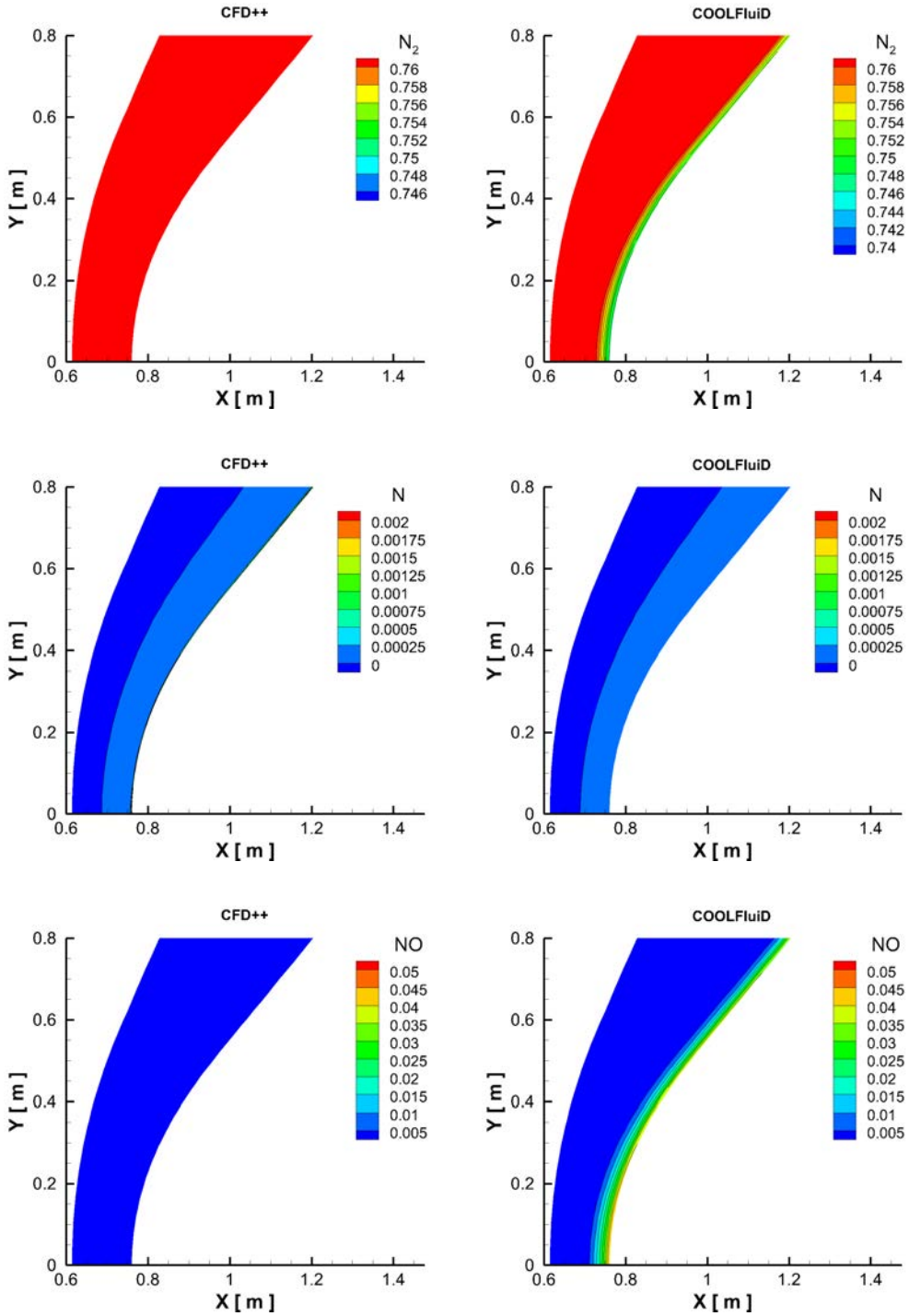

Figure 3.12: *Distribution of the N_2, N and NO species mass fractions for the Mach 10 case with isothermal boundary condition at the vehicle surface (T_w=1000 K): comparison between CFD++ and COOLFluiD.*

At Mach 25 the two curves agree quite well in the stagnation region, but they start to diverge at the beginning of the flat bottom part (around $x = 1$ m). In particular, the heat flux profile in COOLFluiD starts increasing again after the stagnation region, and it forms a curvature in the central part of the wall, while the heat flux computed by CFD++ decreases monotonically. At around $x = 2.5$ m a strong decrease in both the solutions occurs, but a gap between the curves is still present. This jump is a consequence of a fluid expansion, due to the particular vehicle geometry which forms a convex corner at this point. In the Mach 10 case there is in general a better agreement between the two profiles, which overlap each other almost in every zone. It is worth noticing that in the center part now the curves follow both a linear trend, moreover the heat transfer peak at the corner becomes more visible.

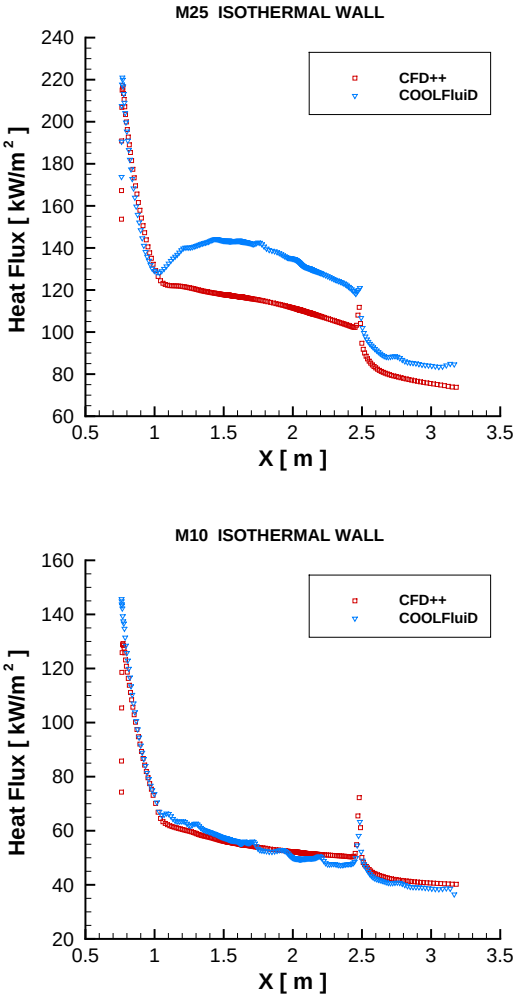

Figure 3.13: *Heat flux profiles along the vehicle surface for the Mach 25 and Mach 10 cases with isothermal boundary conditions (T_w=1000 K): comparison between CFD++ and COOLFluiD.*

These two graphs can be read considering the previous qualitative comparisons in temperature and species distributions. In fact, it is possible to see that the regions where the most relevant differences in temperature and gas compositions occur are the same in which the higher disagreements in the heat flux are found.

Taking into account the more realistic condition of a radiative equilibrium surface, at Mach 25 a better agreement is found in the temperature field solution, which is now colder compared to the isothermal case, because energy is dissipated by radiation. An improvement is evident also in the temperature at the stagnation region (Figure 3.14) and in the populations involving nitrogen (Figure 3.15).

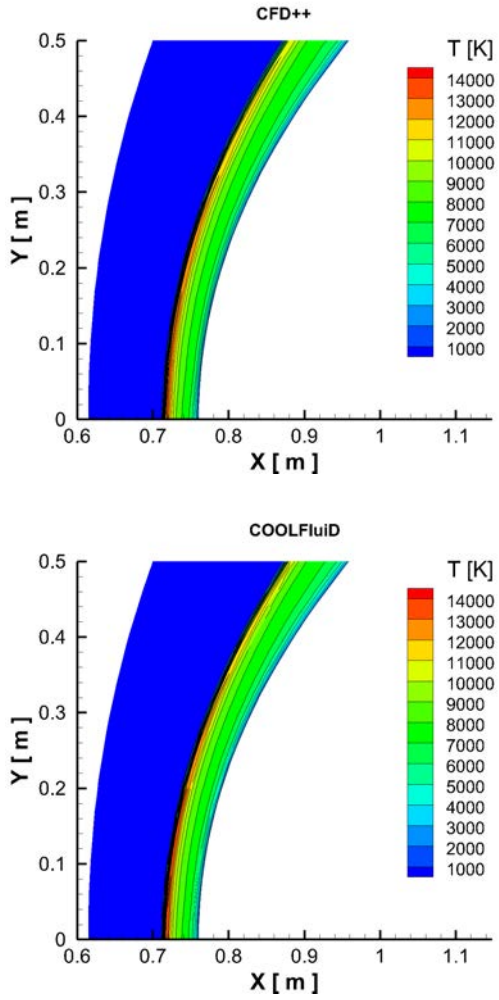

Figure 3.14: *Zoom of the temperature field at the stagantion region for the Mach 25 case with radiative equilibrium boundary condition at the vehicle surface: comparison between CFD++ and COOLFluiD.*

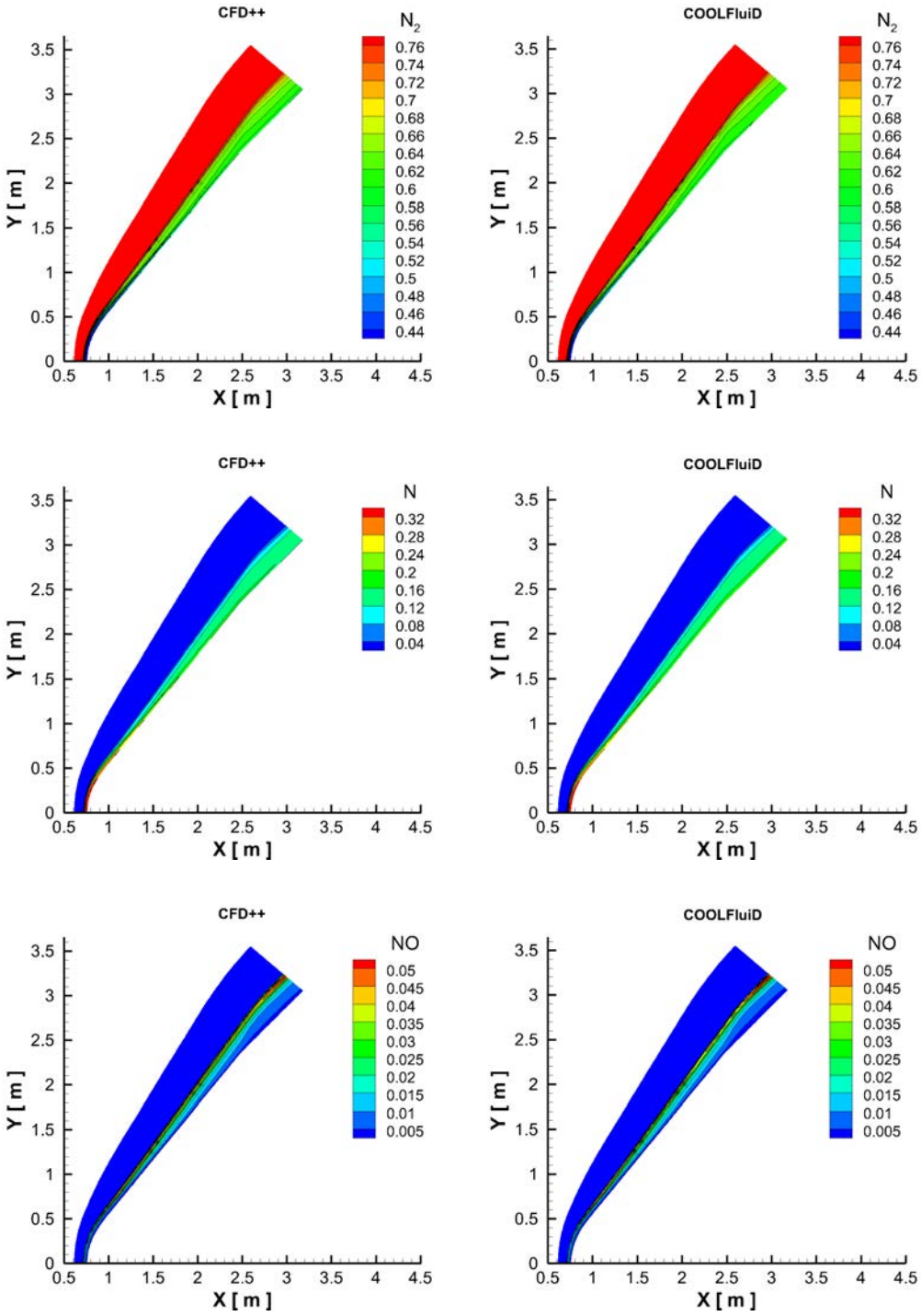

Figure 3.15: *Distribution of the N_2, N and NO species mass fractions for the Mach 25 case with radiative equilibrium boundary condition at the vehicle surface: comparison between CFD++ and COOLFluiD.*

Nevertheless, at the wall, temperature and heat flux profiles do not coincide (Figure 3.16). The surface temperature follows the same trend in both the codes, but in COOLFluiD the curve is shifted upwards by 100 K. According to CFD++, in the central part of the vehicle the temperature at the surface is about 1200 K, while at the stagnation it reaches 1370 K. Also the heat flux profiles disagree: the one computed by COOLFluiD maintains the curvature in the central part as in the isothermal case, with the same difference of about 40 kW/m^2. Moreover, now the two curves differs also in the stagnation region for the same quantity. This because in the isothermal case the imposition of the wall temperature and the local equivalence in the mixture composition led to the same conditions in this part of the field.

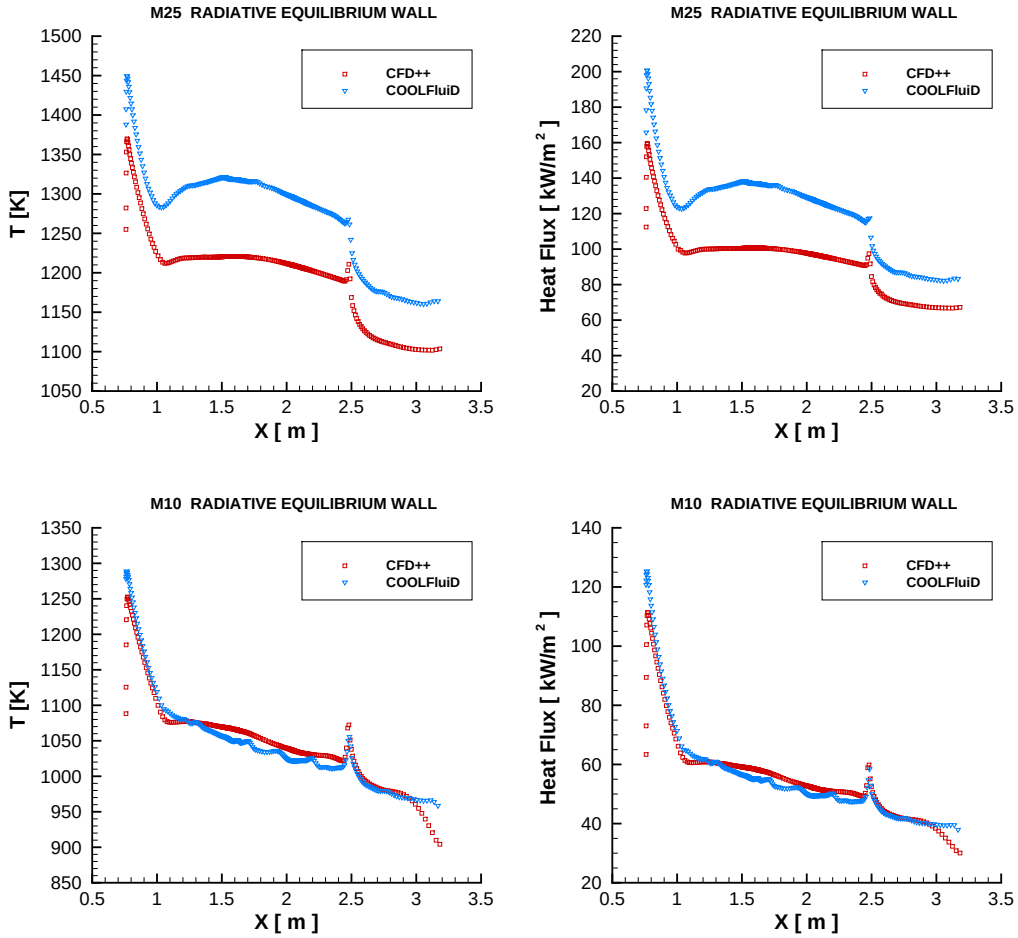

Figure 3.16: *Temperature and heat flux profile along the vehicle surface for the Mach 25 and 10 cases with radiative equilibrium boundary condition: comparison between CFD++ and COOLFluiD.*

In radiative equilibrium on one side the distribution of all the quantities agree quite

well, but on the other, wall temperature and heat flux are in disagreement. This suggests that the total energy presented in the system could be calculated differently by the two algorithms. In fact, to have the same flow characteristics COOLFluiD has to dissipate more energy. Mach 10 case does not show an inconsistent behavior with the isothermal situation, the same considerations can be done and the wall temperature and heat flux agree quite well.

From the results presented so far, the need of a deeper investigation about the relation between chemistry and wall heat flux is clear. The idea is to understand which species reach the vehicle surface and through which reactions they do it. In fact, the heat flux computation, at given conditions, is not directly related to the mixture composition in the shock layer, but to the mixture composition at the vehicle surface. Thus, considering a wall perpendicular cut through the fluid domain, it is possible to have an idea about the species evolution during the diffusion process from the freestream to the TPS surface. For this purpose, a data extrapolation is done perpendicularly to the wall at the first patch location $x = 1.58$ m, in this way the particles movement due to convection is neglected. In Figure 3.17 the temperature and the species mass fractions along this adimensionalized line are collected for the Mach 10 and 25 cases in radiative equilibrium conditions. From the graphs it can be seen that at Mach 10 the two software identify the same trend for the temperature and the air species. The temperature is constant across the shock layer, it has a small increment close to the boundary and then it decreases. This is in agreement with the fact that the chemical reactions occur only close to the vehicle surface, where in small quantity N_2, and mostly O_2 dissociate. As a result more atomic oxygen and a small amount of nitric oxide are present there, while the atomic nitrogen is never found across the fluid domain. At Mach 25 the fluid has a huge kinetic energy in the freestream, which leads to a sudden increment of the temperature at the shock, high enough to activate the chemical reactions, and then it starts to decrease. Oxygen is totally dissociated at the shock, while N_2 disappears more gradually. Also in this case the two models agree quite well, slight differences appear at the wall where CFD++ calculates more N_2 dissociation and more presence of O.

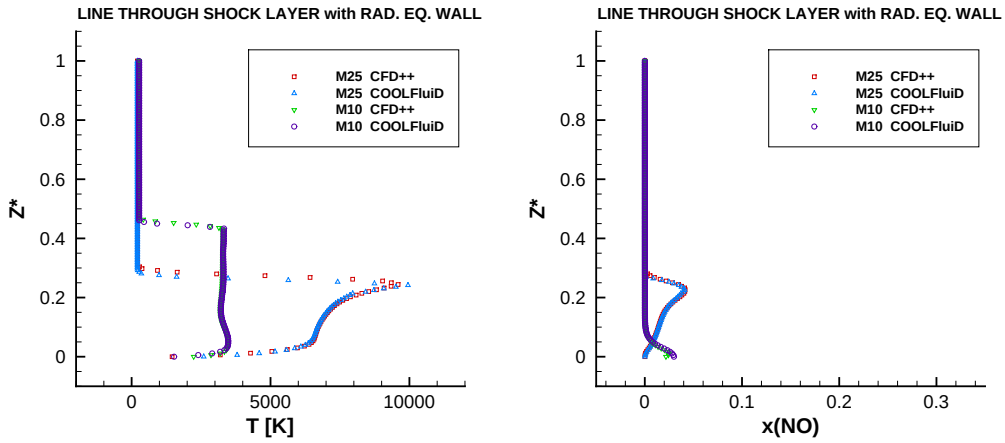

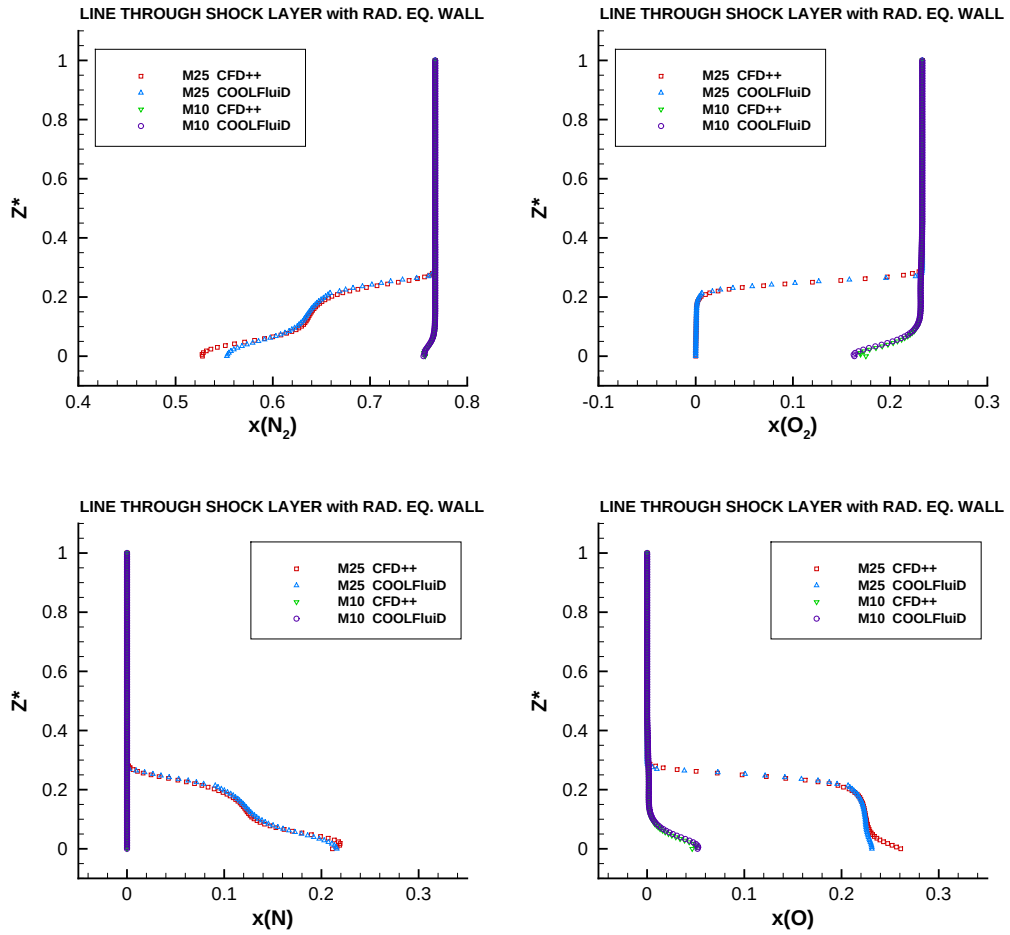

Figure 3.17: *Temperature and species mass fractions evolution along a wall perpendicular line at* $x = 1.58$ *m. Mach 10 and 25 cases with radiative equilibrium boundary condition: comparison between CFD++ and COOLFluiD.*

If the data extraction is made along the stagnation line, it is possible to analyze the flow closer to equilibrium conditions. In fact, in this region the fluid velocity is small and the reactions occur with high rates because the temperature has the highest values. For this reason differences due to the treatment of the chemistry should normally appear with less evidence in this zone. Moreover, diffusion becomes here of paramount importance, given the very low speed. Figure 3.18 shows once again that the species mass fractions agree very well except in the surface proximity. At Mach 10 temperature linearly decreases after the shock. In the stagnation part the entire region between the shock and the nose is chemically active, in fact gas composition continuously changes: N_2 and O_2 dissociate to produce NO and O, while N is not present due to temperatures too low. At Mach 25 instead, temperature drops more drastically after the shock, O_2 immediately disappears and also N_2 dissociates faster compared to Figure 3.17.

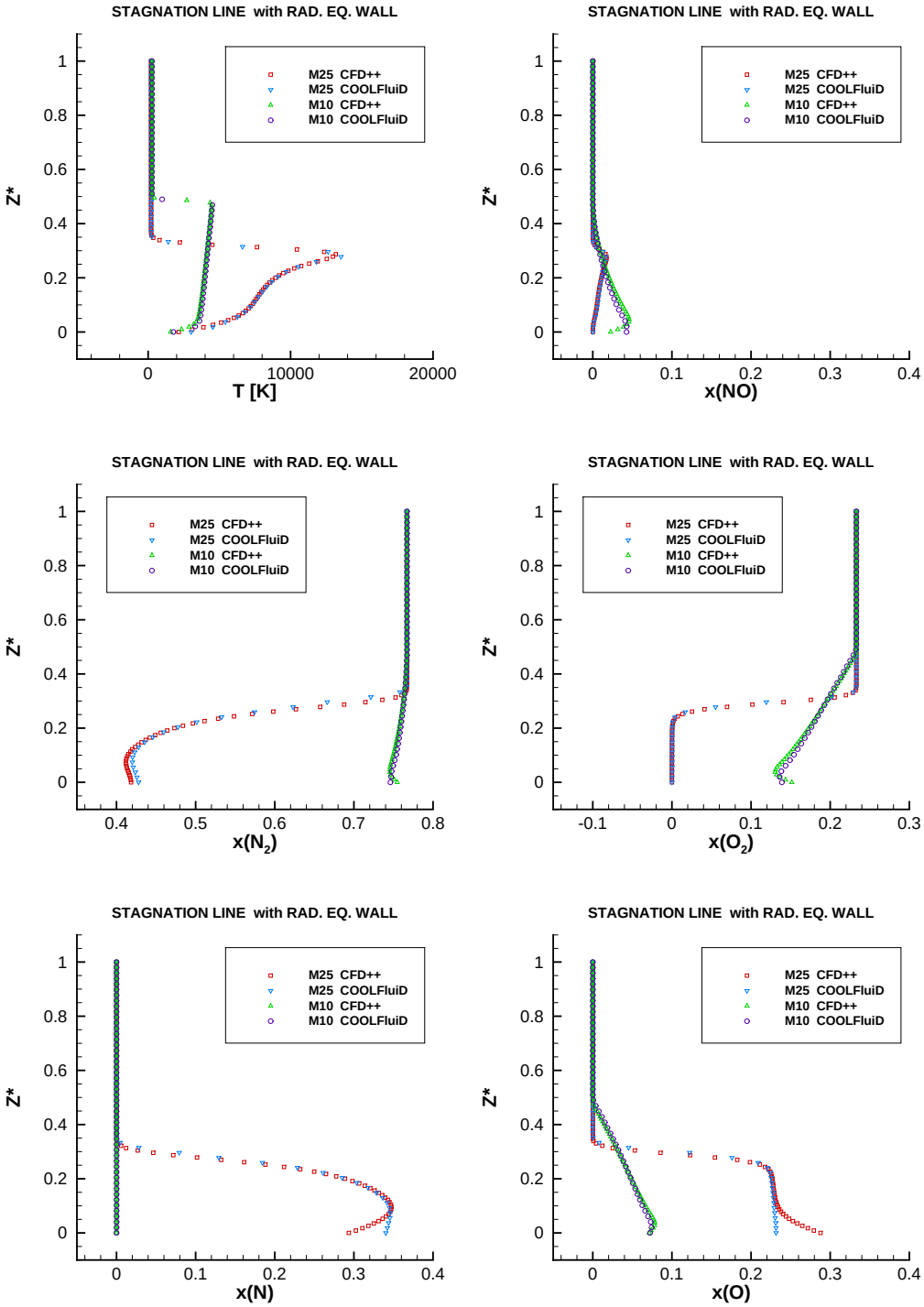

Figure 3.18: *Temperature and species mass fractions evolution along the stagnation line. Mach 10 and 25 cases with radiative equilibrium boundary condition: comparison between CFD++ and COOLFluiD.*

Variations between the two software are evident, once again, only close to the vehicle surface, with a maximum difference in the mass fractions of about 5% of the total mass. More than one evidence has been verified about the models different behavior in the lower part of the boundary layer. In order to understand how much is the variation in the species mass fractions and in which part of the TPS it is more relevant, the species distribution along the entire vehicle surface is plotted in Figure 3.19. It can be seen that for each species the curves follow the same trend along the surface in both the codes. At low Mach mainly the freestream molecular species are present at the wall, and they are distributed quite uniformly along all the surface. On the contrary, at Mach 25 the presence of the atomic species becomes relevant, together with the molecular nitrogen. O_2 and NO instead do not appear. Atomic oxygen is more uniform along the surface, while nitrogen is present in molecular form always in major quantity, even though in the stagnation part it dissociates more and therefore its distribution shows a minimum.

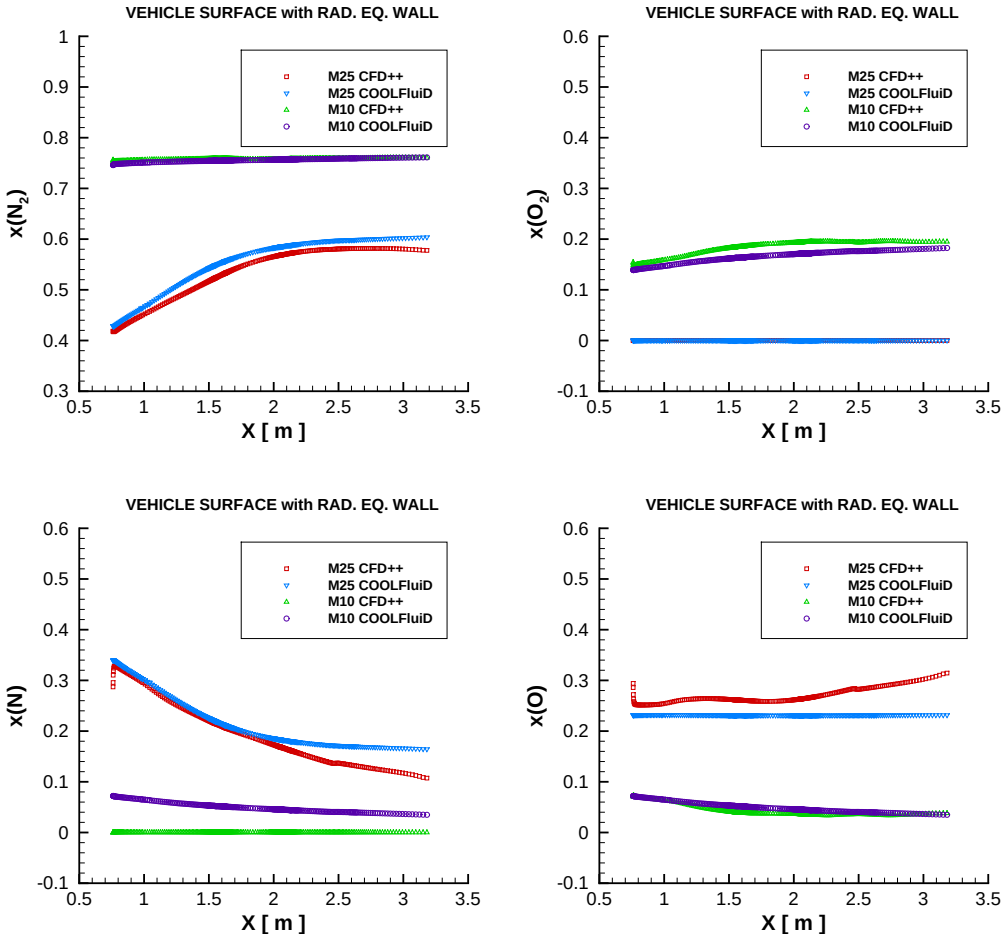

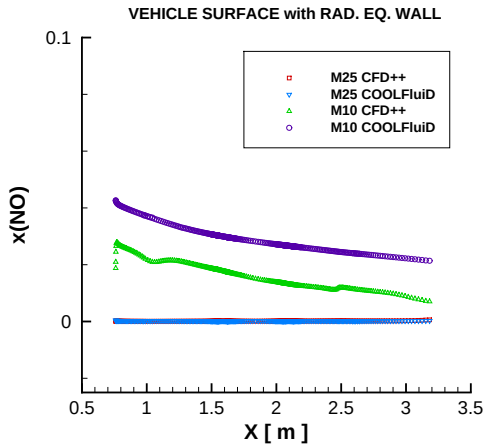

Figure 3.19: *Species mass fraction distribution at the vehicle surface for the Mach 25 case with radiative equilibrium boundary condition: comparison between CFD++ and COOLFluiD.*

Since it is not possible to look directly into the algorithms, it is difficult to clearly understand the reason of the two software disagreement in the heat flux computation. Nevertheless, from the results exposed so far and from the available information, some hypotheses could be done. As it was said in Ch. 2, three physical models are needed to close the system of equations, meaning the description of: chemistry, transport properties and thermodynamic properties. According to the way these aspects are modeled, all of them could affect the final solution. Information about their implementations and the considerations made during the previous discussion may reasonably lead to the following conclusions:

- The chemistry is treated with the same accuracy in both codes, as long as not too extreme conditions are reached. The isothermal case, in fact, disagrees more in comparison to the radiative equilibrium condition, especially in the nitrogen chemistry, which is the most active at high temperatures. In this sense, COOLFluiD calculates more nitrogen dissociation respect to CFD++. The mass fractions extrapolations across the flow field at the patch location and at the stagnation region reveal in general a good agreement between the two software. Exception is made in the confined zone close to the wall, where other aspects become important, i.e. diffusion.

- The transport properties calculation could be responsible of the disagreements in the lower part of the boundary layer, where diffusion is predominant. From the data extrapolation it is clear that particles diffuse in the same way across the flowfield, but in the surface proximity some discrepancies occur. Also, they are more evident at the stagnation point, where pure diffusion drives the flow. Looking at the diffusion flux implementations, it is possible to see that CFD++ uses a Fick's law with a correction for the mass conservation [26], while COOLFluiD uses the Stefan Maxwell formulation which is equivalent at the rigorous definition [2].

- Thermodynamic properties evaluation is fundamental for an accurate estimation of the heat flux component due to the species enthalpy. According to the CFD++ manual [26], for this kind of air model, enthalpy and specific heats are calculated from polynomial interpolation based on NASA tables from McBride et Al. [16], which are suitable for temperature up to 6000 K. For higher temperature values, such as the ones reached at very high Mach number, extrapolations are made leading to inevitable inaccuracy. On the other hand, COOLFluiD calculates the entalphy based on the more accurate data of Gurvich et Al. [9, 10]. Most probably this could be the main responsible of the disagreement between the two codes.

At this purpose, it has to be said that other IXV simulations with CFD++ are found in literature [19], where suitable fitting for high temperature mixture, such as Gupta & Yos [8], have been used instead of the default setting. The results obtained are not far from the one found in this project, in particular they lie between the two solutions computed here by the same software and COOLFluiD. The previous considerations give a reasons of the inconsistencies found in the two software solutions. Even if the VKI research code did not go through a complete process of validation, some comparisons have been made in the past between COOLFluiD and another VKI internal code, COSMIC. The same problem has been tested, giving results in very good agreement. Moreover, external validations have been successfully made also with NASA codes. Thus, it may be said that the COOLFluiD model leads to a more trustworthy solution.

	COOLFluiD		CFD++	
Mach	T [K]	HF [kW/m^2]	T [K]	HF [kW/m^2]
10	1290	130	1250	110
15	1550	260	1460	210
20	1460	220	1400	175
25	1450	200	1370	160

Table 3.2: *Temperature and heat flux maximum values at the stagnation point for different Mach conditions with radiative equilibrium wall and non catalytic effect.*

Finally, the 2D non catalytic study is completed with the collection in Figure 3.20 of the temperature and heat flux profiles for all the different Mach conditions. It is interesting to notice that at Mach 10, when no significant chemistry takes place, temperature and heat flux are quite far from the other curves, which are instead grouped together. The disagreement between the two software is more or less constant for Mach values greater than 10, in particular CFD++ computes values which are around 18% and 25% lower than COOLFluiD, respectively in the flat part and in the stagnation region. From the picture it is clear that the highest heat flux in the flat windward part occur at Mach 25, but in the stagnation region, and in absolute, the most critical conditions are experienced at Mach 15, with temperature around 1550 K and a heat flux of 250 kW/m^2, according to COOLFluiD. This is not surprising, in fact it is known that for a lifting body trajectory

the maximum thermal load occurs at a specific altitude during the re-entry, where the decrease of the vehicle velocity and the increase of the atmosphere density find a critical point (for a shuttle trajectory it is about 70 km of altitude [34]). The maximum values at the stagnation point for the other Mach conditions are collected in Tab. 3.2.

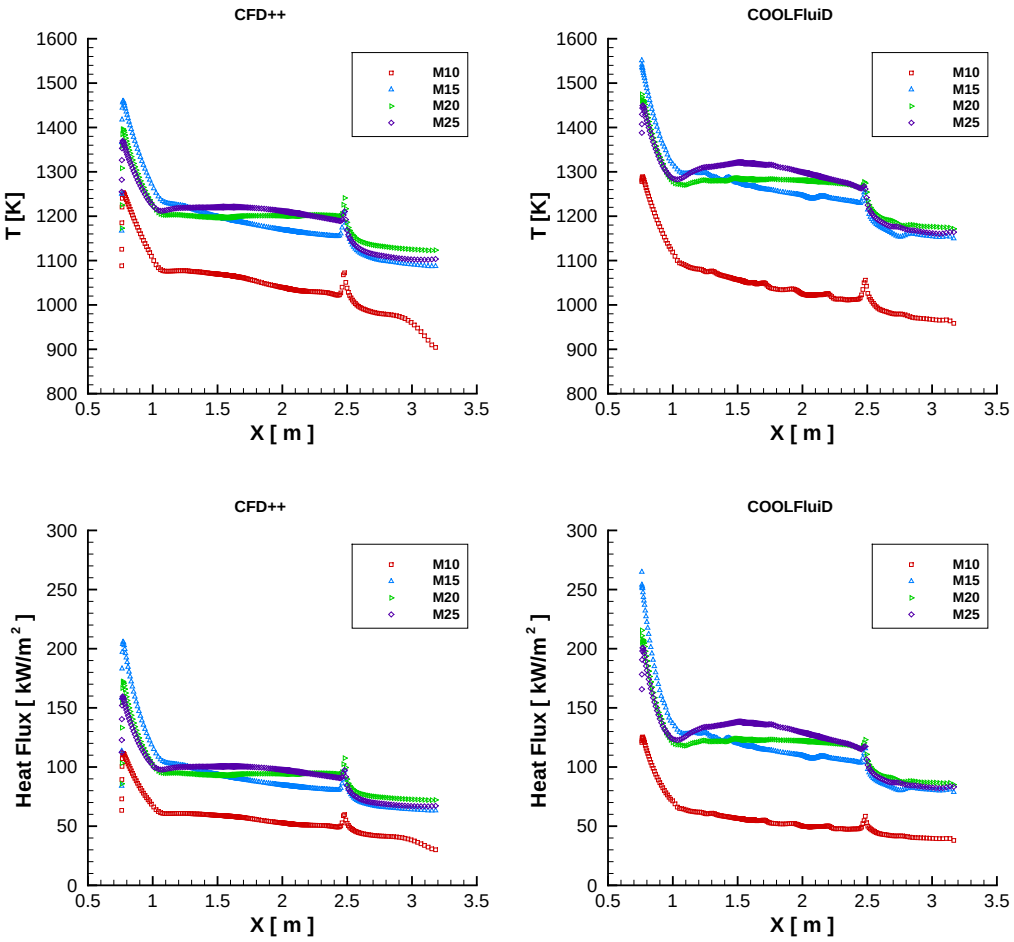

Figure 3.20: *Temperature and heat flux profiles along the vehicle surface for all the Mach conditions with radiative equilibrium boundary condition: comparison between CFD++ and COOLFluiD.*

Chapter 4

2D Study: The Surface Catalytic Effect

In this chapter the catalytic effect at the vehicle surface is introduced. After the phenomenon description and the classification of various surface behaviors, the implementation of the suitable boundary condition is explained. The results for the Mach 20 case are discussed in more details for different catalytic conditions, because this is the regime that will be compared with the 3D simulation. For the other Mach conditions only the heat flux profiles are shown.

4.1 Catalysis and Wall Type Classification

At re-entry conditions the gas in the shock layer is usually dissociated. When "relaxation" in temperature and pressure occurs, atomic species can recombine and energy is released due to the exothermic nature of these reactions. A third body is necessary to make this happens, and it can be an atom or a molecule, but also the vehicle surface. In the former case the reaction is called homogeneous, in the latter heterogeneous. When the vehicle surface is involved the phenomenon is called catalytic surface recombination. As a catalyst, the wall reduces the necessary activation energy of the reactions, hence more collisions lead to recombinations. Accordingly more reaction heat is released.

At the TPS surface different recombination reactions can occur. For wall temperature below 2000-2500 K, they can be classified as follow [18]:

1. Atoms in the gas phase can be adsorbed by a free active surface site (S) or they can leave the surface by thermal desorption (Figure 4.1a). The adsorbed ones are called adatoms. The adsorption-desorption reaction is written as:

$$A + (S) \leftrightarrows (A - S) \tag{4.1}$$

2. Atoms in the gas phase can recombine with adatoms to form a molecule that leaves the surface (Figure 4.1c). This mechanism is called Eley-Rideal (E-R) recombina-

tion, and it is written as:

$$A + (B - S) \rightarrow AB + (S) \tag{4.2}$$

3. Adatoms migrate on the surface and recombine together in a molecule that leaves the surface. This mechanism is known as Langmuir-Hilsenwood or (L-R) recombination (Figure 4.1e).

$$(B - S) + (A - S) \rightarrow AB + 2(S) \tag{4.3}$$

4. Molecules in the gas phase can be adsorbed by a free surface site and released by thermal desorption. Usually this process does not release heat, unless the adsorbed molecule is highly excited. Nevertheless, this mechanism can modify the number of free sites and, therefore, the efficiency of E-R and L-H reactions (Figure 4.1b).

5. Molecules are adsorbed on the surface and dissociated (dissociative adsorption): it is the reverse of the E-R and L-H mechanisms (Figure 4.1d). This process usually does not happen on TPS materials in the temperature range of interest. On the contrary, this reaction can occur for O_2 molecule on metallic surfaces, but it does not apply to this particular problem.

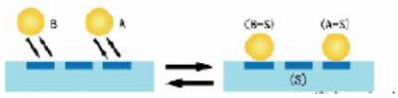

(a) Adsorption and desorption of an atom A and B on a free active site (S).

(b) Adsorption and desorption of a molecule on a free active site.

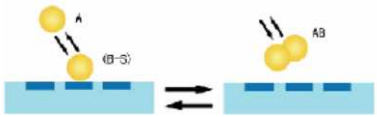

(c) Eley-Rideal recombination and dissociative adsorption of a molecule AB.

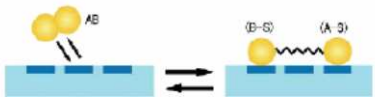

(d) Dissociative adsorption and desorption of a molecule AB on two free active sites.

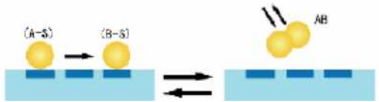

(e) Langmuir-Hilsenwood recombination and dissociative adsorption of a molecule AB.

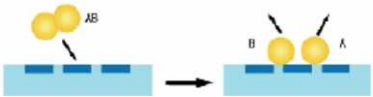

(f) Dissociation reaction of a molecule AB.

Figure 4.1: *Chemical processes in heterogenous catalysis on surface [17].*

Generally, a material can behave differently with respect to the recombination reactions occurring at its surface. Hence, the material catalytic properties play an important

role in the evaluation of the total heat flux at the vehicle TPS. To quantify the rate of recombination, it is useful to define the catalycity or recombination probability γ_i as:

$$\gamma_i = \frac{\mathcal{M}_{i,rec}}{\mathcal{M}_{i,imp}} \tag{4.4}$$

where $\mathcal{M}_{i,imp}$ is the number flux of i species impinging the surface and $\mathcal{M}_{i,rec}$ is the number flux of i species recombining at the surface. The γ parameter depends on the flow conditions and on the type of material. According to the values it assumes, the following definitions can be given [1]:

- *Non catalytic wall* $\rightarrow \gamma_i = 0$. It is a surface whose material is totally inert to the atoms recombination (Figure 4.2a).
- *Partially catalytic wall* $\rightarrow 0 < \gamma_i < 1$. It is a surface where only some particles recombine. In other words, the recombination reactions are catalyzed at a finite rate (Figure 4.2b).
- *Fully catalytic wall* $\rightarrow \gamma_i = 1$. It is a surface that promotes the recombination of all the atoms hitting the surface. Nevertheless, this situation never happens in reality, because the amount of recombined species can not go beyond the local equilibrium conditions. In fact, as a catalyst, the surface material can only help to proceed towards equilibrium faster, but it does not change equilibrium state (temperature, density) and composition of the gas (Figure 4.2c).

Another condition called "Equilibrium catalytic wall" also exists. It represents a surface at which the species mass fractions take the values they would have at the local equilibrium, defined by the local pressure and temperature at the wall. This means the recombination reactions occur at an infinite rate. For many applications (in particular for $T_w < 2000$ K [3]) the equilibrium value of the atomic species concentration is essentially zero at the wall, thus the fully catalytic and the equilibrium wall condition should coincide. Nevertheless, there is an important distinction between the two: at a fully catalytic wall the depletion of all the atomic species is imposed, while at an equilibrium catalytic wall the chemical composition is defined. This means that in the first case the wall chemical composition is a function of the diffusive flux, while in the other the opposite occurs.

4.2 Boundary Conditions

The boundary condition for the species continuity equations, taking into account the catalytic effect of the wall, is written as:

$$\vec{J}_{i,w} \cdot \vec{n}_w = \dot{w}_{i,cat} \tag{4.5}$$

where $\vec{J}_{i,w}$ is the diffusion flux, $\vec{n}_w$ is the normal to the wall pointing into the wall, and $\dot{w}_{i,cat}$ is the wall reaction rate (i.e. the mass of species i produced or destroyed per unit

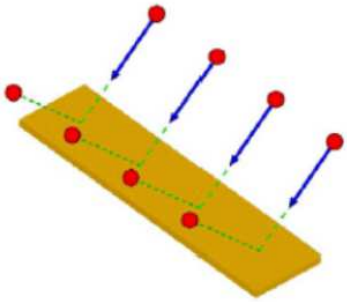

(a) Non-catalytic wall.

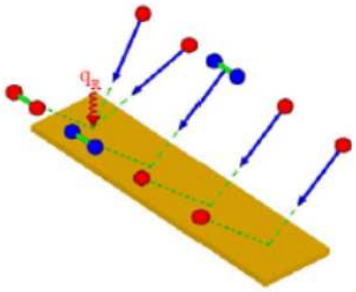

(b) Partially catalytic wall.

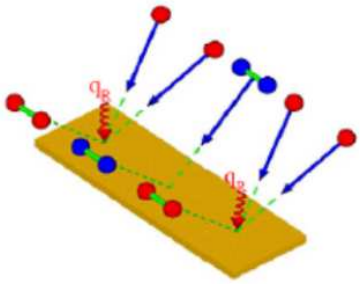

(c) Fully catalytic wall.

Figure 4.2: *Wall type conditions.*

area and per unit time by catalytic reactions). Eq. (4.5) states that, at steady state, the net amount of species i produced or destroyed by catalytic reactions has to be balanced by the diffusion flux of species i itself. In order to evaluate $\dot{w}_{i,cat}$, the recombination probability defined in Eq. (4.4) can be used. The flux impinging the surface is $\mathcal{M}_{i,imp}$, while the one leaving the surface can be written as $\mathcal{M}_{i,imp} - \mathcal{M}_{i,rec} = (1 - \gamma_i)\mathcal{M}_{i,imp}$. Thus, the net flux $\vec{J}_{i,w} \cdot \vec{n}_w$ is equal to the difference of the two multiplied by the i species mass, m_i, leading to:

$$\dot{w}_{i,cat} = \gamma_i m_i \mathcal{M}_{i,imp} \tag{4.6}$$

The expression for the impinging flux $\mathcal{M}_{i,imp}$ is derived from the kinetic theory, and it can take two forms in accordance to the particles distribution function at the wall (for details refer to P. F. Barbante [2]). If the Maxwell distribution is used, the impinging flux is written as:

$$\mathcal{M}_{i,imp} = n_i \sqrt{\frac{kT_w}{2\pi m_i}} \tag{4.7}$$

If instead the Chapmann-Enskog distribution is used, it reads:

$$\mathcal{M}_{i,imp} = n_i \sqrt{\frac{kT_w}{2\pi m_i}} + \frac{1}{2m_i} \vec{J}_{i,w} \cdot \vec{n}_w \tag{4.8}$$

Hence, the wall reaction rates respectively become:

$$\dot{w}_{i,cat} = \gamma_i m_i n_i \sqrt{\frac{kT_w}{2\pi m_i}} \tag{4.9}$$

and

$$\dot{w}_{i,cat} = \frac{2\gamma_i}{2-\gamma_i} m_i n_i \sqrt{\frac{kT_w}{2\pi m_i}} \tag{4.10}$$

The last two expressions are basically identical for $\gamma_i \ll 1$, but they differ for $\gamma_i \to 1$. To be more accurate the second expression should be used because wall reactions perturb the distribution function making it non-Maxwellian.

Values of γ_i can not be measured directly, but they are calculated by numerical solvers using experimental data input. In this case, the wall reacts directly only with the atomic species O and N to form respectively O_2 and N_2. Moreover, the vehicle surface catalytic properties are assumed not to depend on the recombining species, i.e. $\gamma_N = \gamma_O$. For this project γ values for the TPS material and for the patches material are given, and they are collected in Table 4.1. In order to study the catalytic jump effect, the coating on the patches presents higher catalytic properties, in particular it has a γ value which is 10 times greater than the TPS one. It is worth noticing that the recombination probability increases with the Mach number, due to the higher excitation state of the particles.

Mach	γ_{TPS}	γ_{patch}
10	0.00125	0.0125
15	0.00275	0.0275
20	0.00694	0.0694
25	0.01910	0.1910

Table 4.1: *γ values for TPS material and patch material at different Mach conditions.*

4.3 Results

The 2D study of the wall catalytic effect is done at the representative Mach 20 conditions and it starts with the comparison between a non catalytic TPS, and a surface having a homogeneous low catalytic property ($\gamma = 0.00694$). This means that the patches are not considered for the moment, thus at the corresponding boundaries the same γ value of the TPS material is imposed.

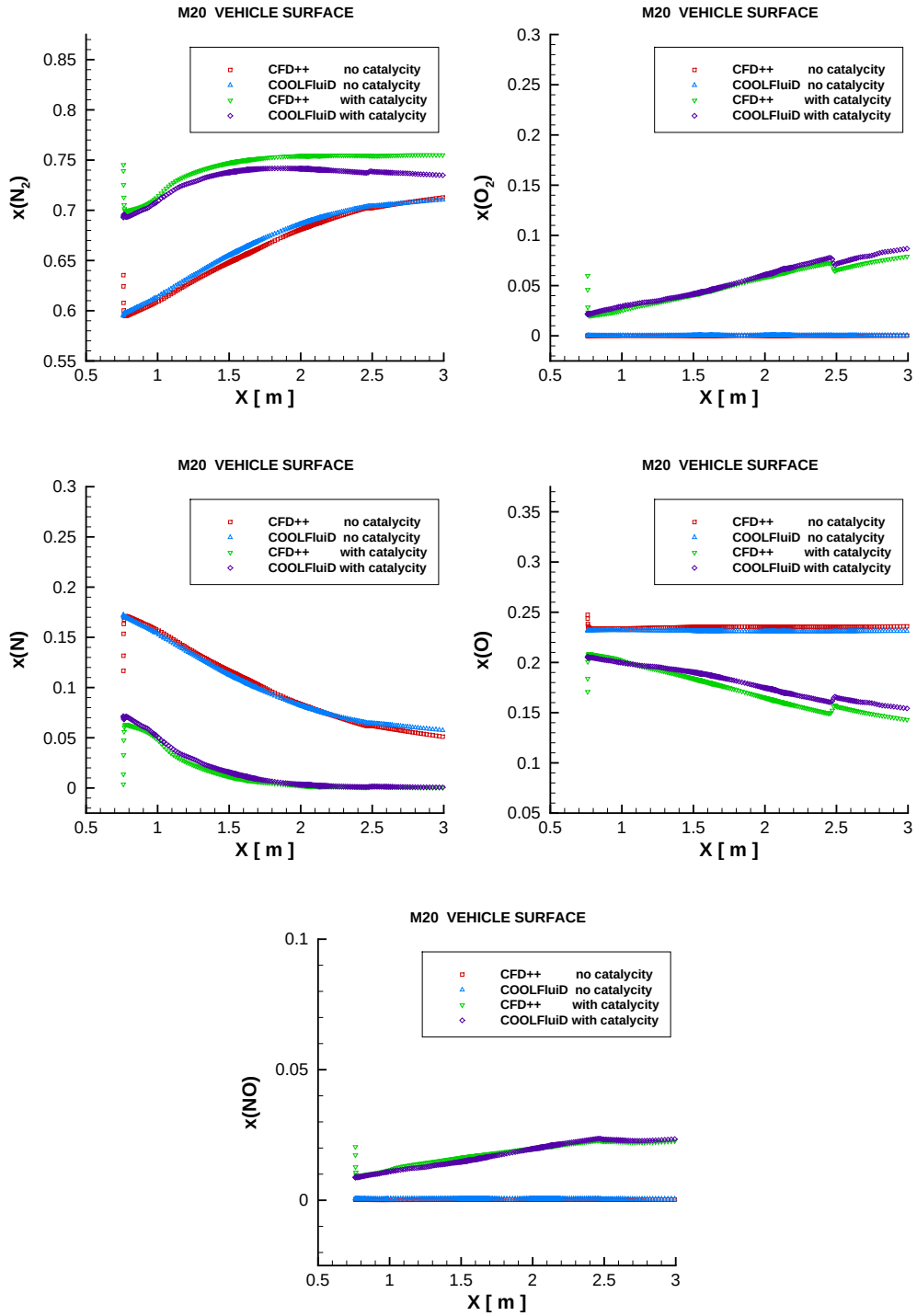

Figure 4.3: *Species mass fraction distribution at the vehicle surface for the Mach 20 case, with and without catalytic effect ($\gamma = 0.00694$): comparison between CFD++ and COOLFluiD.*

In the non catalytic case the mass fraction distributions follow the same trend seen at Mach 25 in the previous chapter. When catalycity is introduced (see Figure 4.3), the effect on the variation of the species quantities is clear. In particular, recombination leads to a reduction of the atomic particles and an increase in the molecular ones. In the stagnation region a lower degree of recombination is experienced, while more molecules are found moving towards the rear part of the vehicle. The most present species are the molecular nitrogen (with values close to the equilibrium ones) and oxygen (mostly in its atomic form). Moreover, it is interesting to notice that the highest variation between N and N_2 appears in the stagnation area, while for oxygen it occurs at the end of the vehicle. This is due both to recombination and diffusion. In fact nitrogen, which is less heavy than oxygen, diffuse easily, so a downstream collection of O_2 more likely occurs. Finally, it has to be noticed that the discrepancies between the two codes are remarkable only in the final part of the vehicle, where other effects become also important. This means that in general the catalytic effect is described with good agreement in both the solutions. The effect of the catalysis has a macroscopic evidence in the temperature and heat flux curves, which are shown in Figure 4.4.

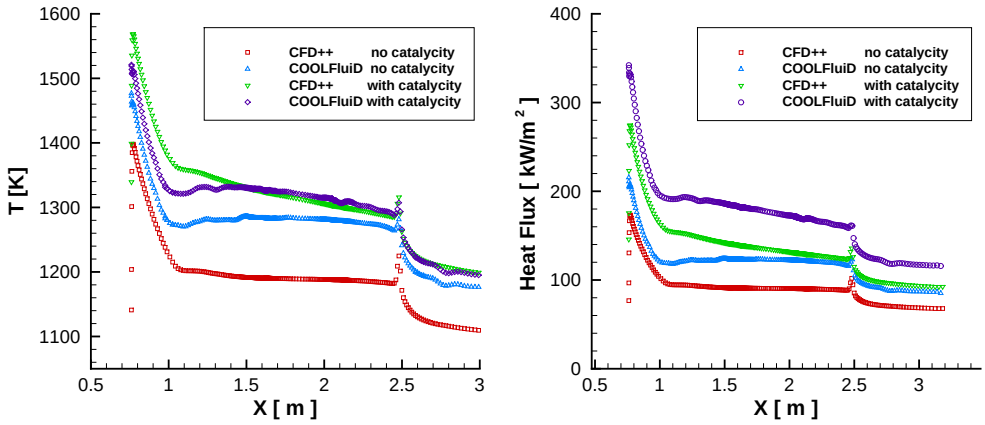

Figure 4.4: *Temperature and heat flux profiles along the vehicle surface for the Mach 20 case, with and without catalytic effect ($\gamma = 0.00694$): comparison between CFD++ and COOLFluiD.*

From the pictures it can be seen that the heat released by the exothermic reactions leads to an increment in the stagnation peak of the temperature profile of about 150 K in CFD++, and 20 K in COOLFluiD, while the heat flux peak shows an increase of 100 kW/m^2 (corresponding to a 57%) in CFD++ and about 110 kW/m^2 (corresponding to a 55%) in COOLFluiD. CFD++ experiences the most drastic variation in the temperature, reaching a peak higher than COOLFluiD. However, the same result is not translated to the heat flux curves: in this case COOLFluiD estimates the highest energy exchange with a 24% increase compared to the CFD++ solution. The peak values in the partially catalytic case, for the other Mach conditions are collected in Table 4.2. When the catalytic phenomenon is introduced, it is interesting to notice that the maximum heat flux peak does

not occur at Mach 15, but it happens at Mach 25. This means that the effect due to the higher recombination probability is bigger than the velocity-density combination effect. In general, the maximum value of heat flux increases with the number of Mach, and the two codes maximum disagreement is found at Mach 15 with a value around 36%.

	COOLFluiD		CFD++	
Mach	T [K]	HF [kW/m^2]	T [K]	HF [kW/m^2]
10	1300	150	1270	120
15	1550	340	1570	250
20	1520	340	1570	275
25	1520	400	1600	300

Table 4.2: *Temperature and heat flux maximum values at the stagnation point for different Mach conditions. Radiative equilibrium wall condition with partially catalytic effect.*

The CATE experiment aims to study the effect of the catalytic jump at the junctions between the base TPS material and the patches material. This is simulated applying the same boundary condition over all the surface, and setting a higher recombination probability locally, at the patches coating. A comparison between the species mass fractions at the TPS, with and without patches, is shown in Figure 4.5. Looking at the pictures, the first evident thing is that a drastic variation in the species distribution occurs in the correspondence of the patches. At the low-high catalytic discontinuities, mass fractions show a local jump, which is then smoothly damped outside the high catalytic zone. Once again oxygen and nitrogen behave differently respect to the catalycity change. It is possible to see that at the first junction a 80% reduction in the atomic oxygen appears, leading to recombinations in O_2 and NO; at the second junction the decrement is lower (around 60%) and it produces more O_2 than NO, compared to the previous jump. Also, it is worth noticing that after the high-low discontinuities the damping does not bring the populations value at the same level found in the case without the patches. In fact, a gap exists because some particles do not diffuse, but are convected downstream (this is the reason why it is less evident in the nitrogen, which has a higher diffusion coefficient). A similar behavior should be expected from the nitrogen chemistry, with a reduction of the atomic species and an increase of the molecular one. On the contrary, the depletion of N is followed by a decrease also in N_2 and a production of NO. This means that the N_2 recombination is followed by the reaction $N_2 + O = NO + N$. This happens because the gas chemistry, active in all the boundary layer, is predominant over the reactions imposed by the catalytic effect.

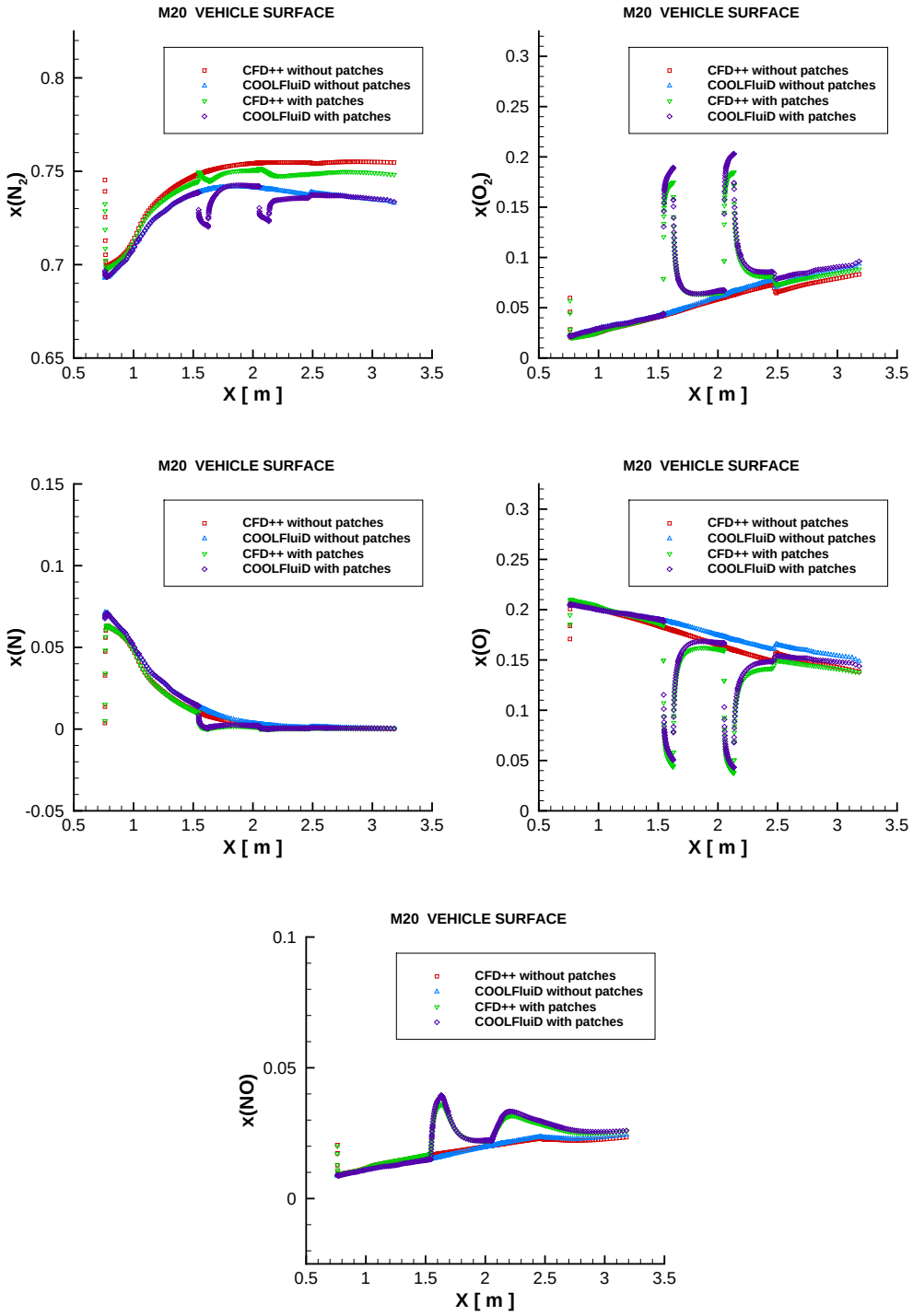

Figure 4.5: *Species mass fraction distribution at the vehicle surface for the Mach 20 case, with and without highly catalytic patches ($\gamma_{TPS} = 0.00694$, $\gamma_{patch} = 0.0694$): comparison between CFD++ and COOLFluiD.*

In other words, catalysis accelerates the nitrogen recombination reactions, but at the same time local conditions make the formation of NO faster, determining the final result shown in the graphs. The two models agree quite well in the high catalytic zones except for the molecular nitrogen. Here a disagreement in the catalytic jump effect has to be summed to the differences already present in the case without the patches: COOLFluiD reveals indeed a bigger amount of N_2 consumption.

At macroscopic level the jump in the TPS catalytic properties leads to the temperature and heat flux solutions given in Figure 4.6. The sudden variation of the species mass fractions finds a correspondence in the jump also in the temperature and in the heat flux curves. In the temperature case only CFD++ shows the discontinuities, while COOLFluiD keeps a smooth profile. This anomaly in the research code was already known, and it is probably due to an error in the post processing visualization of this quantity, because this temperature trend is not physical, as experiments showed [22]. In CFD++ on the first patch the temperature increases of 220 K, reaching the same level of the stagnation peak (about 1560 K); on the second junction the temperature difference in the jump is the same, but a lower maximum value is reached (about 1520 K). The commercial code behaves in the same way also regarding the heat flux: the increment on the first patch reaches the stagnation peak at 280 kW/m^2, corresponding to a 100% local variation. On the contrary COOLFluiD reveals a discontinuity up to 440 kW/m^2, much higher than the relative stagnation peak (340 kW/m^2), which is equivalent to a 120% local variation. It is interesting to notice that a small jump occurs also at the high-low catalycity discontinuity, with a clearer evidence in COOLFluiD.

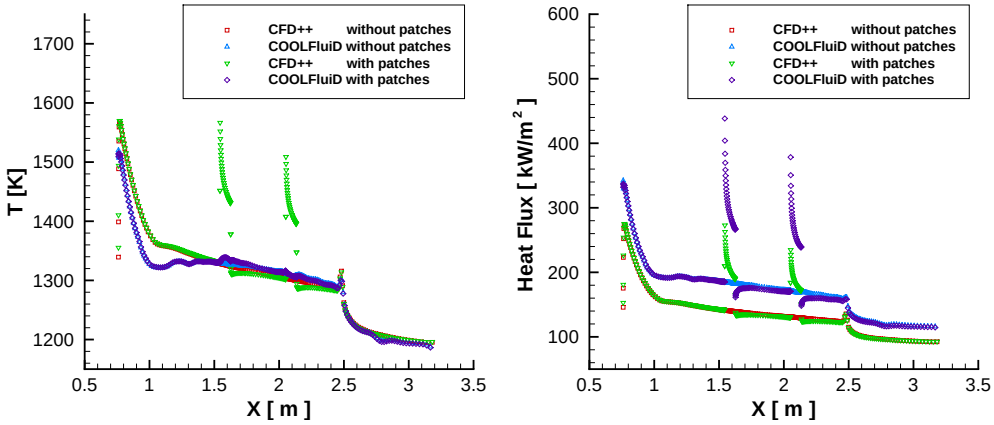

Figure 4.6: *Temperature and heat flux profiles along the vehicle surface for the Mach 20 case, with and without high catalytic patches ($\gamma_{TPS} = 0.00694$, $\gamma_{patch} = 0.0694$): comparison between CFD++ and COOLFluiD.*

A simulation with a fully catalytic wall, meaning a γ factor equal to 1, is also run. As in Figure 4.5, it is evident in this case the overall chemistry effect. Figure 4.7 shows that, despite the imposition of the only N_2 and O_2 recombinations, also NO is produced

driven by the other chemical rates.

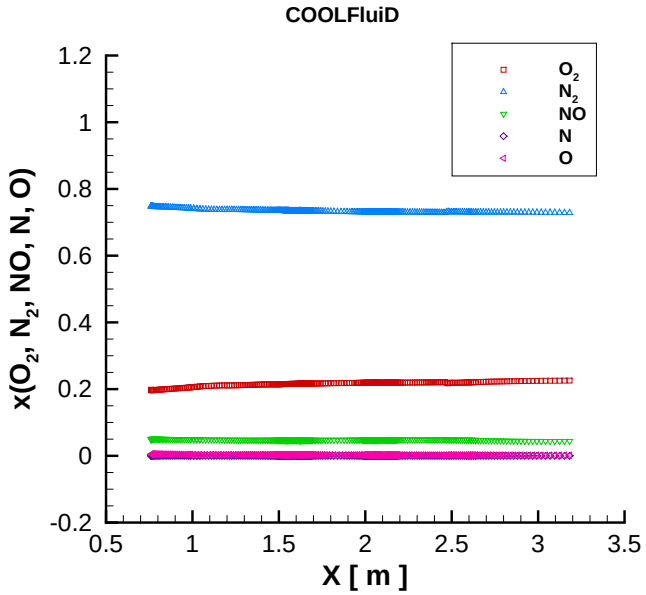

Figure 4.7: *Species mass fraction distribution at the vehicle surface for the Mach 20 case with fully catalytic wall ($\gamma = 1$).*

In order to analyze the influence of the catalytic effect at the Mach variation, Figure 4.8 reports a COOLFluiD comparison of the curves for non catalytic, partially discontinuous catalytic and fully catalytic conditions, at different regimes. The TPS catalytic effect becomes more important as the Mach increases: the difference in the stagnation heat flux between zero and partially low catalytic conditions goes from 7% at Mach 10, to 100% at Mach 25, while with fully catalytic surface the increment goes from 60% to 215%. The catalytic jump enhances the heat flux on patches to higher values than the ones obtained with a homogeneous γ, even if a fully catalytic wall boundary condition is imposed. Physically this happens because, at the junctions between TPS and patches, more atoms are available for recombination with discontinuos partially catalytic conditions rather than with fully catalytic wall. In fact, with $\gamma = 1$ all atomic species start to be consumed by recombination already in the stagnation region, so fewer reach the junctions. Thus, the discontinuous change in the material properties leads to a sudden recombination of a considerable amount of atoms, with a local massive release of energy and so heat flux. The peak of the jump increases with the Mach number, and at Mach 25 it exceeds the relative stagnation peak, leading to a 125% local heat flux variation. Nevertheless, the peak maximum values do not have a pure physical meaning, but numerical aspects affect it. Refining the junction between patches and TPS, in fact, would cause a further increment in the heat flux jump: the sharp temperature discontinuity and the small cells size would make the derivative tend to infinity. For the sake of completeness the results from CFD++ are collected in Figure 4.9.

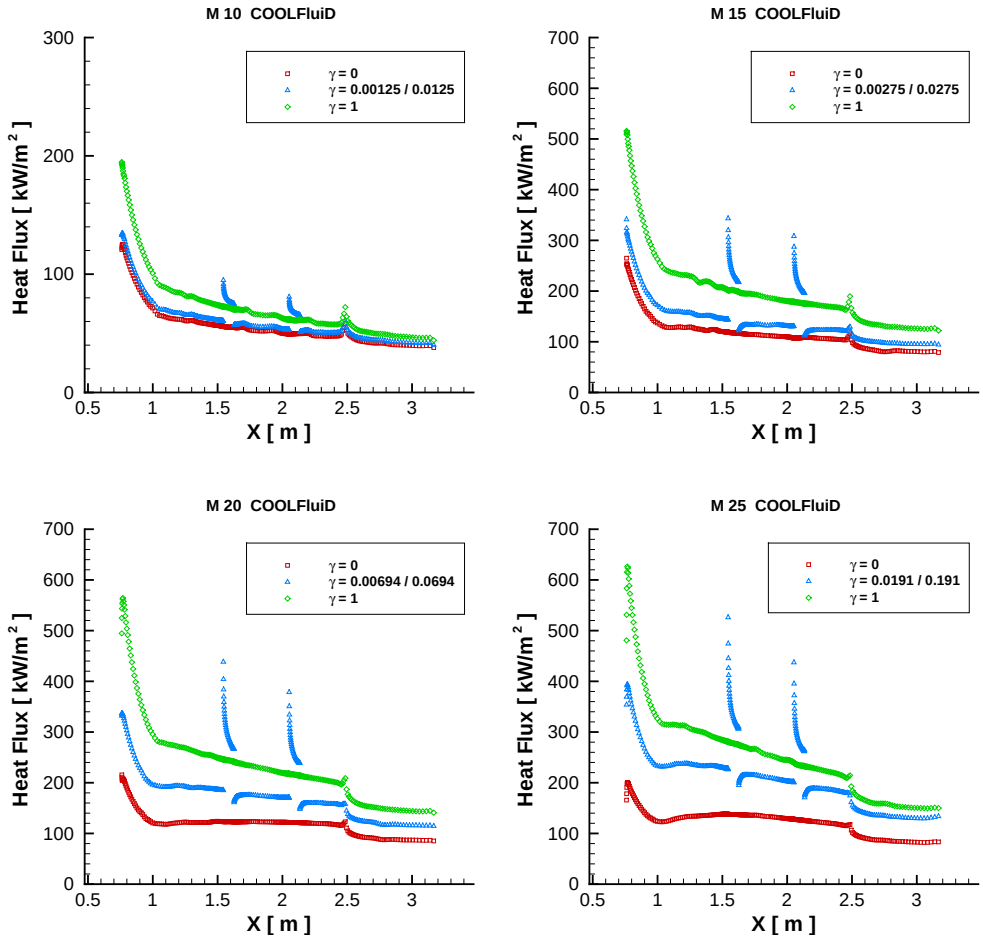

Figure 4.8: *Heat flux profile along the vehicle surface for different Mach conditions, with zero, partially and fully catalytic effect: COOLFluiD results.*

	COOLFluiD		CFD++	
Mach	T [K]	HF [kW/m^2]	T [K]	HF [kW/m^2]
10	1300	200	1360	150
15	1520	520	1700	370
20	1580	570	1750	425
25	1600	630	1870	550

Table 4.3: *Temperature and heat flux maximum values at the stagnation point for different Mach conditions. Radiative equilibrium wall condition with fully catalytic effect.*

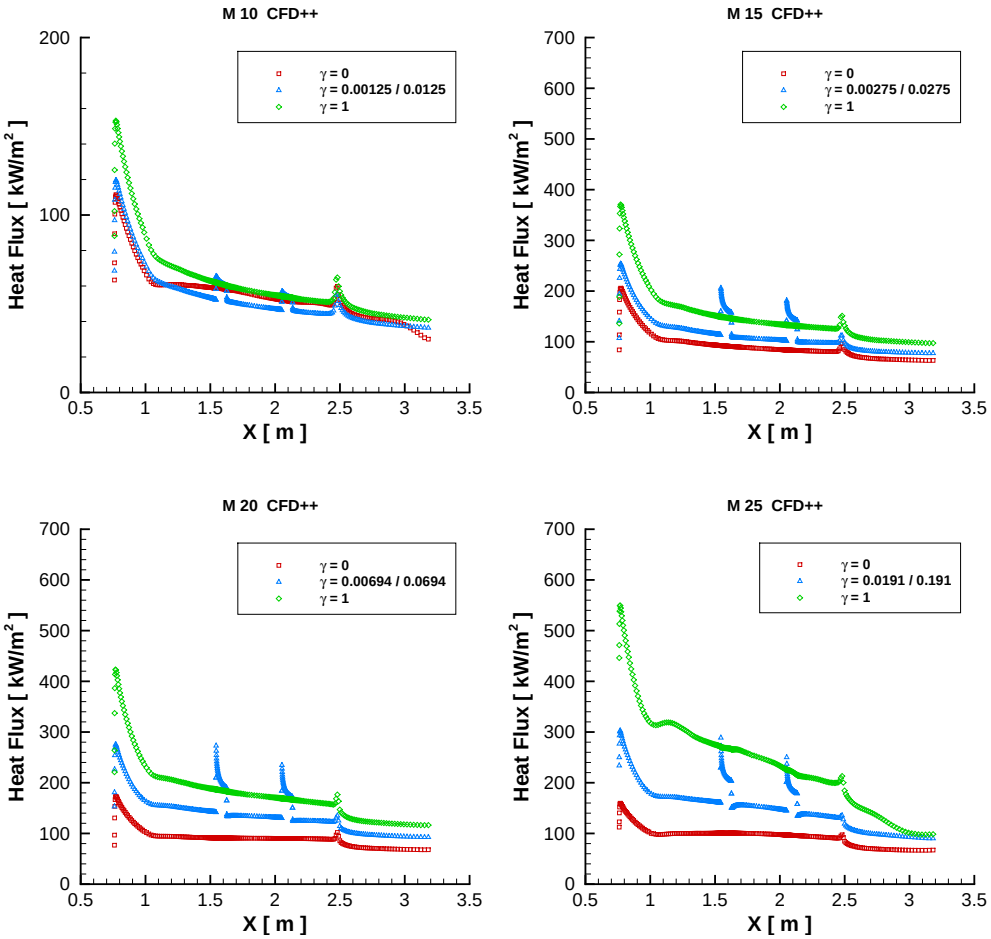

Figure 4.9: *Heat flux profile along the vehicle surface for different Mach conditions, with zero, partially and fully catalytic effect: CFD++ results.*

	COOLFluiD			CFD++		
Mach	$\tilde{\gamma}/\gamma_0$	γ_1/γ_0	$\gamma_1/\tilde{\gamma}$	$\tilde{\gamma}/\gamma_0$	γ_1/γ_0	$\gamma_1/\tilde{\gamma}$
10	7%	60%	33%	9%	36%	25%
15	36%	108%	53%	19%	76%	48%
20	55%	159%	68%	57%	143%	55%
25	100%	215%	58%	88%	244%	83%

Table 4.4: *Increment in the stagnation peak of the heat flux for different catalycity conditions: zero catalycity (γ_0), partially catalycity ($\tilde{\gamma}$) and fully catalycity (γ_1).*

	COOLFluiD		CFD++	
Mach	patch1	patch2	patch1	patch2
10	67%	50%	27%	33%
15	112%	129%	75%	80%
20	120%	111%	83%	77%
25	125%	110%	76%	73%

Table 4.5: *Local increment in the heat flux at the low-high catalytic discontinuities.*

4.4 2D Study Conclusions

The results presented in Ch.3 and Ch.4 about the complete 2D study, can be summarized in the following conclusions:

- The two aerothermodynamic models show disagreements in the evaluation of the temperature and the heat transfer at the surface of the IXV vehicle. Comparison of thermodynamic quantities and species distributions, together with the available information about the specific algorithms implementations, suggests that these discrepancies could be due to differences mainly in the diffusion flux calculation and in the enthalpy computation. The data used to evaluate the latter suggest that this could be probably the primary cause of the solutions discrepancies.

- The heat flux on the vehicle TPS, in conditions of radiative wall equilibrium without catalytic effect, shows a maximum value at the stagnation point at Mach 15, while on the flat bottom part the maximum occurs at Mach 25. The highest value at the vehicle nose computed by COOLFluiD is around 250 kW/m^2, while CFD++ gives 200 kW/m^2, leading to a difference of 25%.

- The introduction of a low catalytic TPS leads to a general uniform increment of the heat flux, due to the energy released by the exothermic recombination reactions occurring at the vehicle surface. The maximum value is found at Mach 25, and it is equal to 400 kW/m^2 in COOLFluiD and 300 kW/m^2 in CFD++. The maximum discrepancy between the codes is about 36% and it occurs instead at Mach 15.

- The catalytic jump simulation reveals a discontinuity in the heat flux at the junctions between the TPS base material and the high catalytic patches. The energy transfer increases with the Mach number, and it can exceed also the stagnation heat flux peak. It has to be said that the jump maximum value does not depend only on the physics. In fact, refining locally the junction would give a higher local peak, because the enhancement of the temperature discontinuity would lead to an increase in the derivative. In reality the heat flux peak is not as sharp as the simulated one, also because the catalytic properties on the TPS junction do not vary so drastically. This is particularly true if it is considered that the high catalytic coating is applied through a deposition process.

Chapter 5

3D Study

A 3D study is made in order to check if the results of the 2D simulations are representative of the phenomenon occurring in the 3D space. The final solution is obtained by means of a grid convergence study in non catalytic conditions and in partially catalytic conditions with catalytic jump. The analysis is done using the commercial software CFD++, because more indicated to perform a set of time demanding simulations, characterized by millions of elements.

5.1 Mesh Generation

The 3D mesh is built using a CAD model of the vehicle, whose back part is cut at the point where the flat bottom forms a convex corner. The body is placed inside a fluid domain, whose shape is modeled following the expected shock wave. Only five boundary regions are defined in this case: inlet, outlet, wall, patch1 and patch2, whose identification in Figure 5.1 is evident.

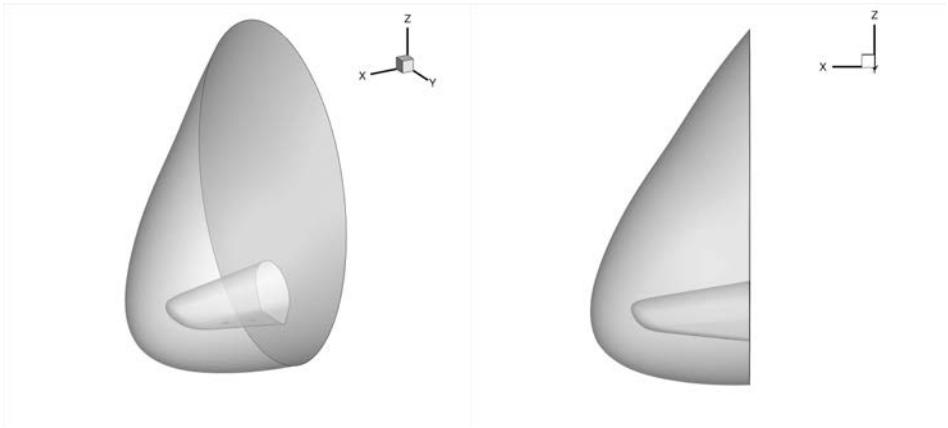

(a) Perspective view. **(b)** Lateral view.

Figure 5.1: *Visualization of the 3D domain.*

No symmetry conditions are necessary in the full size 3D case. The frame of reference

is posed in the back part of the vehicle with the x-axis pointing towards the nose, the z-axis towards the upper part and the y-axis to complete the triad. The boundary conditions imposed are the same discussed in the 2D investigation. The only 3D adaptation is the setting of the freestream velocity at the inlet: the velocity vector has a zero y component, a negative x component and it forms a 45° angle with the x-axis. The mesh is created using a block strategy, and it is formed by hexahedral elements. In order to perform a grid convergence study, a first simulation is run with a mesh having 2.5 million of elements, then a progressive refinement is applied and solutions are obtained with 5 and 7.5 million of elements. Since the first attempt, particular attention is payed in refining the critical zones around the two patches, and the boundary layer around the vehicle surface. As it will be shown, further refinements are needed in order to correctly capture the shock wave around IXV, and improve in this way the solution. For this reason the number of elements is finally increased to 10 million. The mesh details are collected in Figure 5.2.

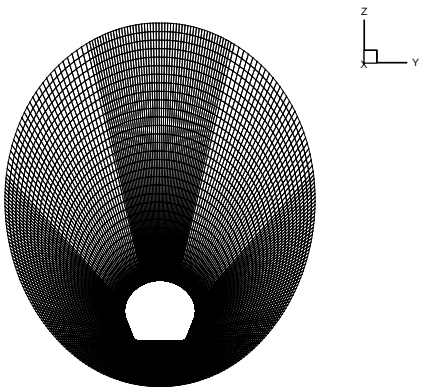

(a) Outlet.

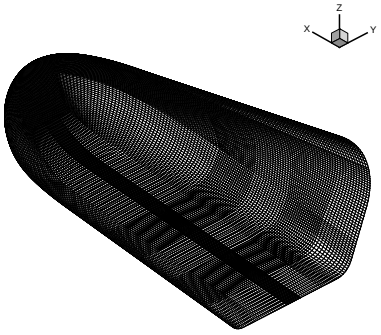

(b) Vehicle surface: bottom perspective view.

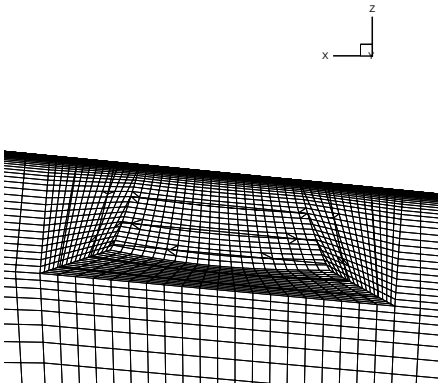

(c) Patch and boundary layer.

Figure 5.2: *Details of the 3D mesh.*

5.2 3D Results

The first convergence study is made for a non catalytic surface. Three refinements are adopted up to 7.5 million of elements. In order to compare the solutions with the 2D results, the temperature and heat flux quantities are extracted along the intersection between the body surface and the perpendicular plane passing through the center line of the patches ($Y = 0.039$ m).

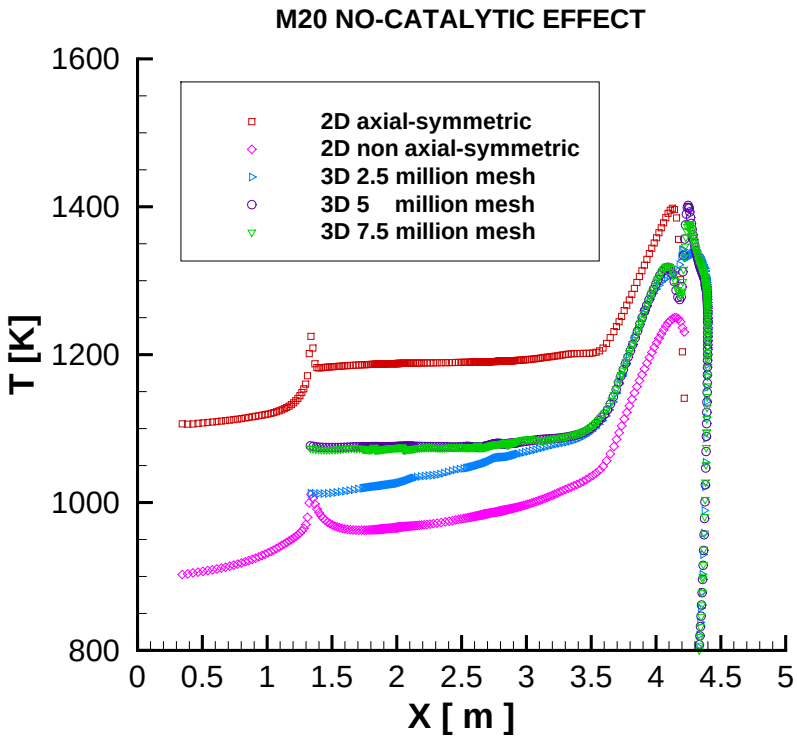

Figure 5.3: *Temperature profile at Mach 20 without catalytic effect: comparison between the 2D and 3D solutions with different mesh refinements.*

The solution from a 2D simulation without axis-symmetric condition is added to the comparisons displayed in Figure 5.3 and 5.8. The graphs show that there is a convergence of the 3D solution: the curves corresponding to the 5 and 7.5 million mesh overlap each other along the entire extracted profile, while the solutions from the coarser mesh disagree on the stagnation peak and on the windward part of the vehicle, giving lower values. It is interesting to notice how the 3D final results reach the same values of the 2D axial-symmetric solution at the stagnation point, but on the rest of the IXV bottom part the curves lay between the 2D axial-symmetric and non axial-symmetric curves.

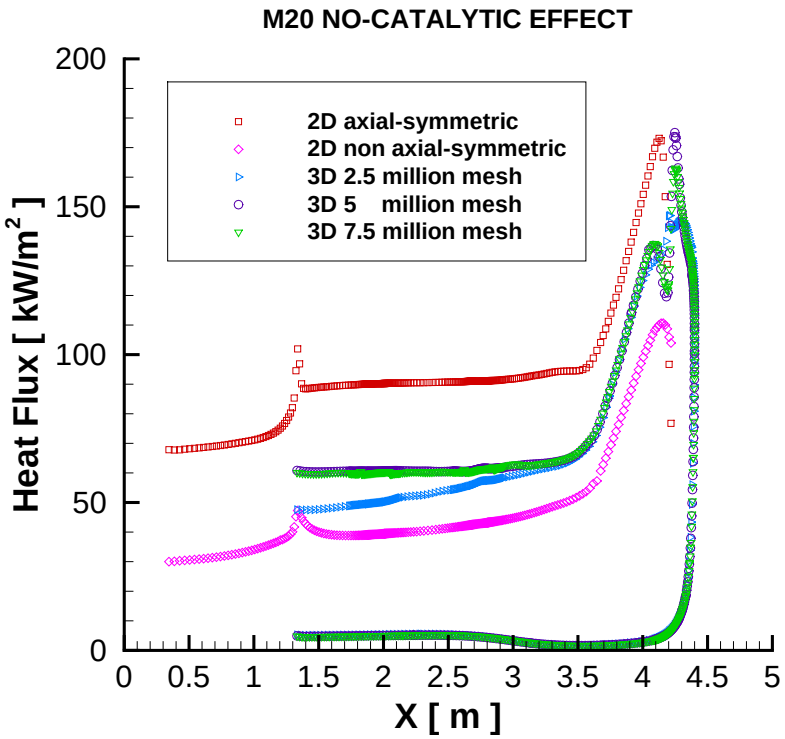

Figure 5.4: *Heat flux profile at Mach 20 without catalytic effect: comparison between the 2D and 3D solutions with different mesh refinements.*

In Sec. 3.2 the meaning and the difference between these two conditions have already been discussed. According to the vehicle geometry, the behavior of the 3D solutions is reasonable. In fact, the windward part does not have a conic shape, as described by the axial-symmetric simulation, and can not be considered either totally flat. The gas indeed turns around the lateral edges of the vehicle, so the shock wave is closer to the wall, compared to an infinitely wide ramp configuration. This is clearly seen in the comparison between the 2D and 3D shock positions reported in Figure 5.5. It can be noticed that the 3D shock wave lies closer to the axial-symmetric case rather than the other one, even if the 3D temperature and heat flux have an average value between the two 2D solutions. Moreover, the coincidence of the shock position in the stagnation region, between the 3D and the axial-symmetric case, explains the agreement in the peak temperature and heat flux, in fact in this zone the surface curvature is small. The 3D temperature peak reaches 1400 K at the nose, while on the windward part it is constant around 1075 K, leading to a difference of 12% compared to the 2D axial-symmetric curve. On the other hand, the heat flux shows a maximum peak around 170 kW/m^2, while at the flat bottom it has a constant value of 60 kW/m^2, corresponding to a 50% decrease compared to the 2D.

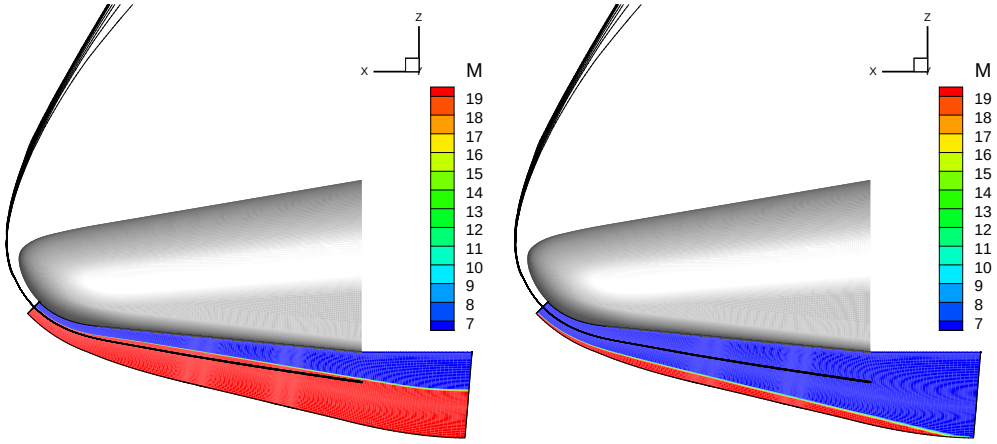

(a) 2D axial-symmetric. **(b)** 2D non axial-symmetric.

Figure 5.5: *Comparison of the shock position in the 2D and 3D solutions at Mach 20 with radiative equilibrium wall.*

The influence of an eventual crossflow is checked by comparing the magnitude of the x and y velocity components (Figure 5.6), and the heat fluxes along the center line of the vehicle and along the center line of the patches (Figure 5.7).

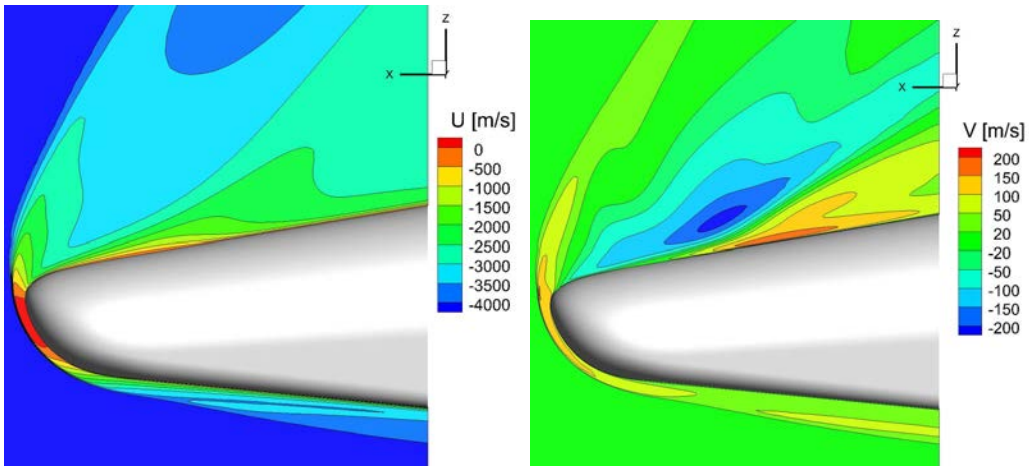

(a) x component. **(b)** y component.

Figure 5.6: *Velocity components in the $Y = 0.039$ m plane, at Mach 20 with radiative equilibrium wall.*

The difference in the velocity components magnitude is relevant in the windward part:

the transverse flow in this zone has a maximum velocity component in the y direction, which is about 5% of the main flow direction velocity. A divergence angle of around 12-10° can be estimated for the stream-traces on the bottom TPS. This is reflected on the heat fluxes comparison in Figure 5.7, where it is evident that the difference between the curves increases as the rear part of the vehicle is approached. However, this variation can be considered negligible, thus the virtual position of the patches on the vehicle center line is reasonable in the 2D study.

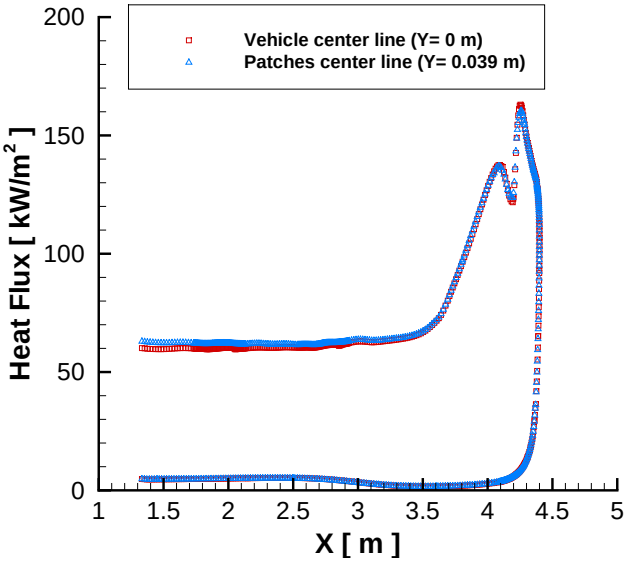

Figure 5.7: *Crossflow influence at Mach 20 with radiative equilibrium wall: comparison between the heat fluxes along the vehicle and the patches center lines.*

Looking at the curve profiles at the stagnation point, it has to be noticed that an anomalous double peak occurs in all the 3D extrapolations. This is due to the formation of non physical hot and cold zones on the vehicle nose, which gives a not reasonable pattern of the heat flux. In order to fix this problem, adjustments in the grid are necessary. In particular a re-orientation of the cells and a refinement are done around the shock position. In this way the entropy introduced in the system is reduced, leading to an improvement in the heat flux evaluation. These modification are applied to study the catalytic effect and the catalytic jump phenomenon in the 3D case. To confirm the solution convergence also in this new aspects implementation, simulations are run with the previous 5 and 7.5 million mesh and with a 10 million mesh, result of the discussed refinements. The comparison between the 2D and 3D temperatures and heat fluxes is shown in Figure 5.8. The same considerations done in the non catalytic case about the curves positions can be applied to the catalytic study too. In particular this is true also for the temperature and heat flux jumps on the two patches. The temperature peak at the stagnation has a value of 1600 K, while in the flat part it is around 1225 K, corresponding to a 6% reduction compared to the 2D axis-symmetric case.

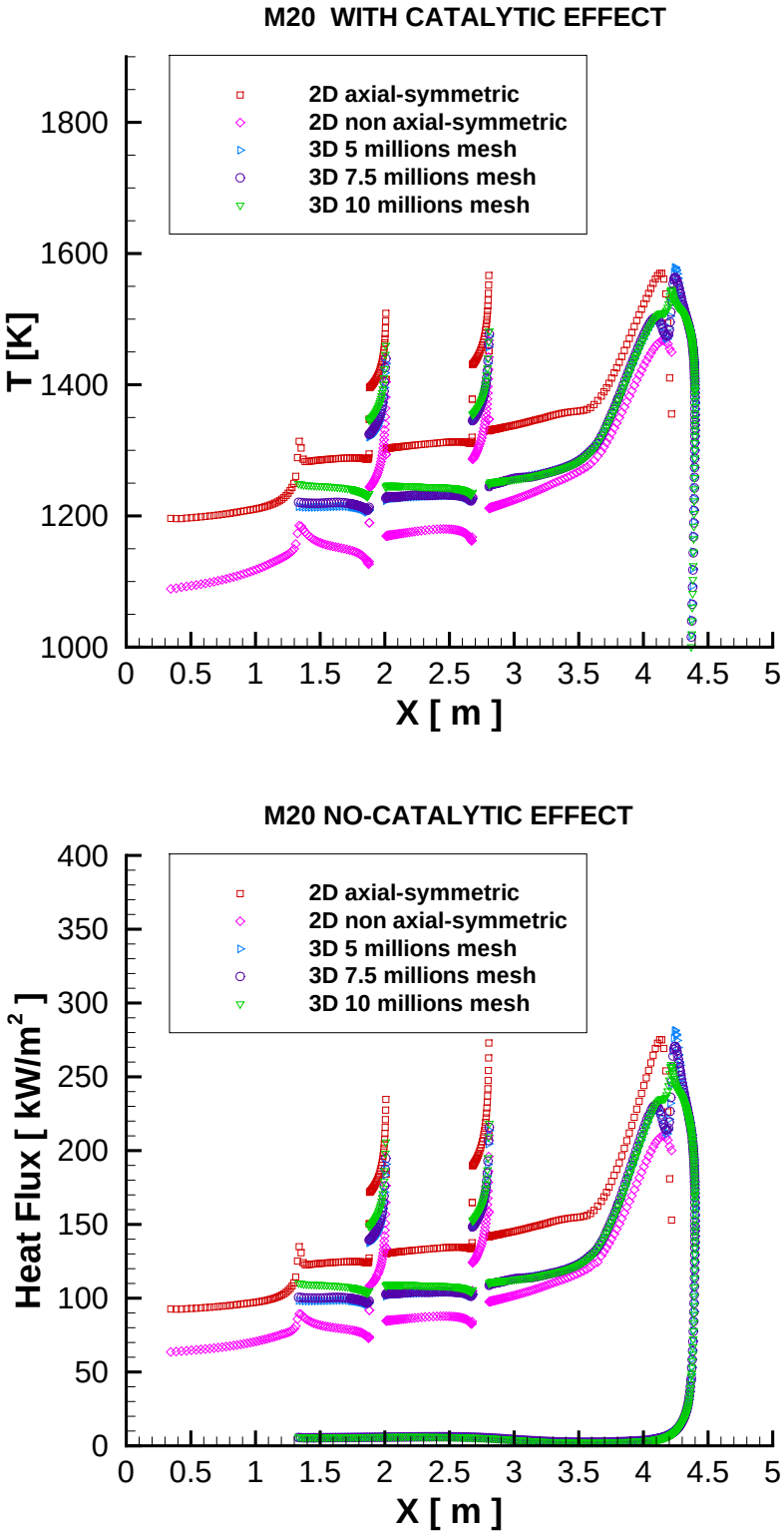

Figure 5.8: *Temperature and heat flux profiles at Mach 20 with catalytic effect: comparison between the 2D and 3D solutions with different mesh refinements.*

The heat flux instead shows a maximum value at the stagnation of 250 kW/m^2, and 100 kW/m^2 on the rest part of the TPS. The jumps have respectively a maximum value of 220 kW/m^2 and 210 kW/m^2, leading to a difference of of 23% and 14%, compared to the 2D axis-symmetric case. In the 3D simulation the first discontinuity in the heat transfer does not reach the stagnation peak level, as it happens in 2D, but the two jumps are more homogeneous. It is worth noticing how the shock refinement improves the solution at the stagnation peak, which is now more smooth. Finally, the Mach and pressure plots are shown to have a whole idea of the 3D re-entry phenomenon.

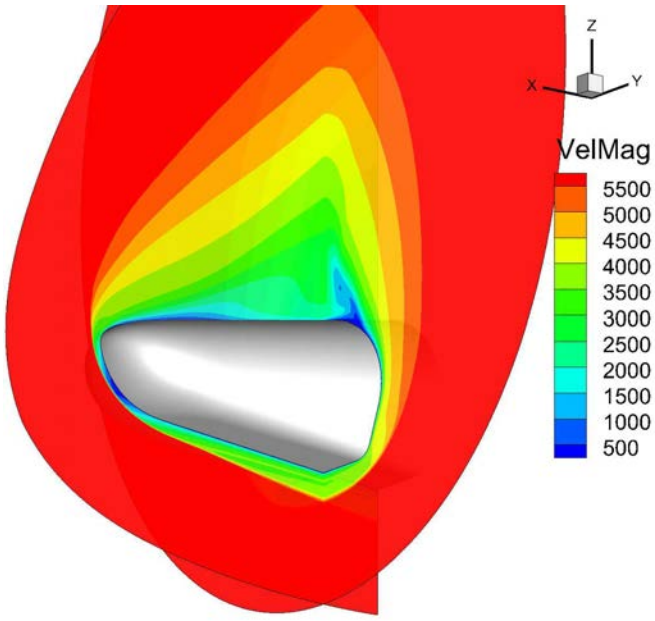

Figure 5.9: *Mach distribution on two slices at $x = 1.93$ m and $y = 0$ m at Mach 20 with radiative equilibrium wall.*

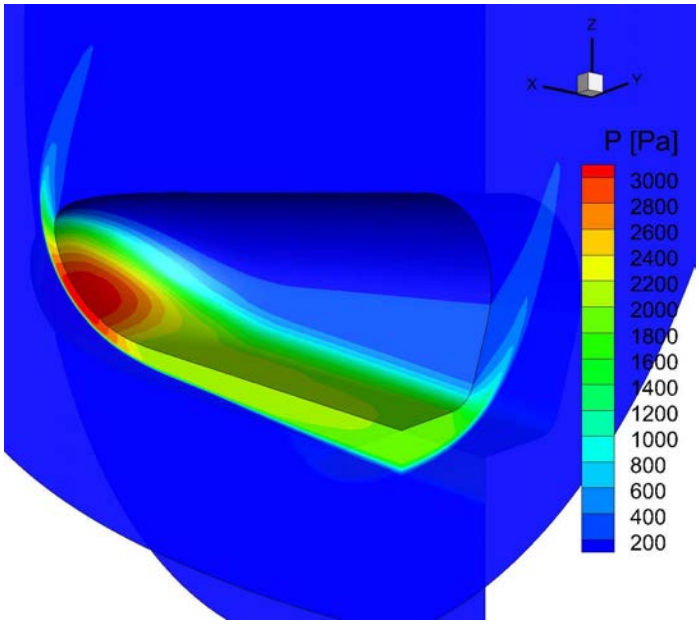

Figure 5.10: *Pressure distribution on two slices at $x = 1.93$ m and $y = 0$ m at Mach 20 with radiative equilibrium wall.*

Chapter 6

Conclusions

In this work a numerical study of the surface catalytic effect and the catalytic jump effect has been done for different Mach conditions, using the commercial code CFD++ and the VKI research code COOLFluiD. The investigation started considering some simplified cases, in which wall isothermal conditions and non catalytic effects are applied, in order to better identify eventual software disagreements. The surface catalytic effect is than introduced, with and without discontinuity in the atomic recombination probabilities, testing all the Mach conditions with both codes. Finally, a 3D grid convergence study is made using only CFD++, for comparison with the 2D solution.

The results achieved in this project can be summarized as follow:

- The preliminary study revealed some inconsistencies between the software solutions. In particular, COOLFluiD computes higher values of wall temperatures and heat flux compared to CFD++. More than one factor seems to be the cause of these disagreements: difference in the transport and thermodynamic properties evaluation could be probably the main reason. Limitations in the CFD++ air properties fits and successful comparison of COOLFluiD with other VKI and NASA algorithms may lead to consider the research code solution more trustworthy.

- It has been shown that the catalytic effect of the surface changes the species distribution on the vehicle TPS, leading to a higher amount of recombined molecules. This increases the overall heat flux, producing increments on the stagnation peak of about 100% in COOLFluiD and 88% in CFD++. The maximum disagreement between the software is about 25%, in the case of no catalycity, and 36% if the catalytic effect is considered.

- The catalytic jump was correctly simulated even if the peak values computed do not have a pure physical meaning, due to the numerical implementation of the phenomenon. Nevertheless, even if the peak was increases due to refinements, the relaxation zone would have converged to common values in the final part of the patch, leading to a not negligible gap at the high-low catalytic discontinuity.

- The comparison between the 2D and the 3D simulations showed that the 2D axis-symmetric condition gives the same heat flux stagnation values, while on the rest part of the TPS its solution is in an acceptable range to be considered a suitable overestimation.

This project should be considered a first step towards a more accurate and physical simulation of the catalytic jump effect. Future works should take into account the implementation of more suitable strategies to describe in a more realistic way the heat jump at the low-high catalytic discontinuities. One of these possibilities could be, for example, the implementation of a transition between the low and high catalytic properties by means of a continuous γ variation at the patches junction locations.

Bibliography

[1] J. D. Anderson. *Hypersonic and High Temperature Gas Dynamics*. Reston, VA: American Institute of Aeronautics and Astronautics, 2006.

[2] P. F. Barbante. “Accurate and Efficient Modelling of High Temperature Nonequilibrium Air Flows”. PhD Thesis. Von Karman Institute for Fluid Dynamics/Institute National Polytechnique de Toulouse, 2001.

[3] Giordano D. Barbato M. and J. Muylaert. “Comparison of Catalytic Wall Conditions for Hypersonic Flow”. In: *Journal of Spacecraft and Rockets* 33.5 (1996).

[4] J. J. Bertin. *Hypersonic Aerothermodynamics*. Washington: American Institute of Aeronautics and Astronautics, 1994.

[5] Park C. *Nonequilibrium Hypersonic Aerothermodynamics*. New York: John Wiley & Sons, 1990.

[6] S. Chapman and Cowling T. G. *The mathematical Theory of Non-Uniform Gases*. Cambridge University Press, 1970.

[7] J. H. Ferziger and H. G. Kaper. *Mathematical Theory of Transport Processes in Gases*. North Holland, 1972.

[8] Yos J. M. Gupta R. N. and R. A. Thompson. *A review of Reaction Rates and Thermodynamics and Transport Properties for an 11-Species Air Model for Chemical and Thermal Nonequilibrium Calculations to 30000 K*. Report 1232. NASA, 1990.

[9] Veyts I.V. Gurvich L.V. and C.B. Alcock. *Thermodynamic properties of individual substances, volume 1: O, H(D,T), F, Cl, Br, I, He, Ne, Ar, Kr, Xe, Rn, S, N, P, and their compounds, Part one: methods and computation, Part two: tables*. Hemisphere, 1989.

[10] Veyts I.V. Gurvich L.V. and C.B. Alcock. *Thermodynamic properties of individual substances, volume 2: C, Si, Ge, Sn, Pb, and their compounds, Part one: methods and computation, Part two: tables*. Hemisphere, 1991.

[11] E. H. Hirschel. “Aerothermodynamics of Radiation-Cooled Surfaces”. In: *Aerothermodynamics of Propulsion Integration for Hypersonic Vehicles*. Ed. by AGARD. 1996.

[12] E. H. Hirschel. *Basics of Aerothermodynamics*. Heidelberg: Springer-Verlag, 2005.

[13] A. Lani. *User manual for the Finite Volume Aerothermodynamics (ATD) solver*. Von Karman Institute for Fluid Dynamics. 2013.

[14] T.E. Magin and G. Degrez. “Transport algorithms for partially ionized and unmagnetized plasmas”. In: *Journal of Computational Physics* 198 (2004), pp. 424–449.

[15] Rochelle W.C. Kirk B.S. Marichalar J.J. and C.H. Campbell. “BLIMPK/Streamline Surface Catalytic Heating Predictions on the Space Shuttle Orbiter”. In: *44th AIAA Aerospace Sciences Meeting*. Ed. by AIAA. 2006.

[16] Heimel S. Ehlers J. G. McBride B. J. and S. SGordon. *Thermodynamic Properties to 6000 K For 210 Substances Involving the First 18 Elements*. SP-3001. NASA, 1963.

[17] Walpot L. Ottens H. Muylaert J. and F. Cipollini. “Aerothermodynamics Reentry Flight Experiments Expert”. In: *Flight Experiments for Hypersonic Vehicle Development*. Ed. by Educational Notes RTO-EN-AVT-130. 2007.

[18] Barbato-M. Nasuti F. and C. Bruno. “Material-Dependent Catalytic Recombination Modeling for Hypersonic Flows”. In: *J. of Thermophysics and Heat Transfer* 10.1 (1996), pp. 131–136.

[19] Onofri-M.-Cardillo-D. et al. Paciorri R. “Numerical Assessment of Wall Catalytic Effects on the IXV Surface”. In: *6th European Symposium on Aerothermodynamics for Space Vehicles*. Ed. by H. Lacoste and L. Ouwehand. 2008.

[20] Van Der Haegen-V. Paneari F. and O. Chazot. “Design of CATE, the IXV CATalysis Experiment”. In: *7th European Symposium on Aerothermodynamics*. Ed. by L. Ouwehand. 2011.

[21] F. Panerai. “Aerothermochemistry Characterization of Thermal Protection System”. PhD Thesis. Von Karman Institute for Fluid Dynamics/Università degli studi di Perugia, 2012.

[22] M. Panesi. “Physical Models for Nonequilibrium Plasma Flow Simulations at High Speed Re-entry Conditions”. PhD Thesis. Von Karman Institute for Fluid Dynamics/Università degli studi di Perugia, 2009.

[23] R. E. Sheldal and E. L. Winkler. *Effect of Discontinuities in Surface Catalytic Activity on Laminar Heat Transfer in Arc-Heated Nitrogen Streams*. TND-3615. NASA, 1965.

[24] Rakich J. V. Stewart D. A. and M. J. Lanfranco. “Catalytic Surface Effects Experiment on the Space Shuttle”. In: *31st AIAA Thermophysics Conference*. Ed. by AIAA A981-1143. 1981.

[25] Rakich J. V. Stewart D. A. and M. J. Lanfranco. “Effects on Space Shuttle Thermal Protection System During Earth Entry of Flights STS-2 Through STS-5”. In: *Shuttle Performance: Lessons Learned*. Ed. by NASA-CP 2283. 1982.

[26] Metacomp Technologies. *CFD++ User Manual*. 2013.

[27] G. Tumino. *IXV: the Intermidiate eXperimental Vehicle*. Bulletin 128. ESA, 2006.

[28] W. Vincenti and Kruger C. *Introduction to Physical Gas Dynamic*. New York: John Wiley and Sons, 1965.

[29] Zalogin G. N. Lunev V. V. Voinov L. P. and V. P. Timoshenko. “Comparative Analysis of Laboratory and Full-Scale Data on the Catalycity of the Heat Shield for the BOR and BURAN Orbital Vehicles”. In: *Cosmonautics and Rocket Engineering* 2 (1994).

[30] S. D. Williams. *Columbia, the First Five Flights Entry Heating Data Series, Volume 1: an Overview*. NASA CR -171 820, 1984.

[31] S. D. Williams. *Columbia, the First Five Flights Entry Heating Data Series, Volume 3: the Lower Windward Surface Center Line*. NASA CR -171 665, 1983.

[32] Sawley M. L. Wüthrich S. and Perruchoud G. “The Coupled Euler/Boundary-Layer Method as a Design Tool for Hypersonic Re-entry Vehicles”. In: *Zeitschrift für Flugwissenschaften und Weltraumforschung (ZFW)* 20.3 (1996).

[33] I. Yasutoshi. “OREX Flight -Quick Report and Lessons Learned”. In: *Second European Symposium on Aerothermodynamics for Space Vehicles*. Ed. by L. Ouwehand. 1994.

[34] Gupta R. N. Simmonds A. L. Zoby E. V. “Temperature-Dependent Reaction-Rate Expression for Oxygen Recombination at Shuttle-Entry Conditions”. In: *AIAA-Paper 84-0224* (1984).